Publication Year	2019
Acceptance in OA	2020-12-16T11:27:09Z
Title	The Next Generation Virgo Cluster Survey. XXIII. Fundamentals of Nuclear Star Clusters over Seven Decades in Galaxy Mass
Authors	Sánchez-Janssen, Rubén, Côté, Patrick, Ferrarese, Laura, Peng, Eric W., Roediger, Joel, Blakeslee, John P., Emsellem, Eric, Puzia, Thomas H., Spengler, Chelsea, Taylor, James, Álamo-Martínez, Karla A., Boselli, Alessandro, CANTIELLO, Michele, Cuillandre, Jean-Charles, Duc, Pierre-Alain, Durrell, Patrick, Gwyn, Stephen, MacArthur, Lauren A., Lançon, Ariane, Lim, Sungsoon, Liu, Chengze, Mei, Simona, Miller, Bryan, Muñoz, Roberto, Mihos, J. Christopher, Paudel, Sanjaya, Powalka, Mathieu, Toloba, Elisa
Publisher's version (DOI)	10.3847/1538-4357/aaf4fd
Handle	http://hdl.handle.net/20.500.12386/28884
Journal	THE ASTROPHYSICAL JOURNAL
Volume	878

The Astrophysical Journal, 878:18 (25pp), 2019 June 10 https://doi.org/10.3847/1538-4357/aaf4fd

The Next Generation Virgo Cluster Survey. XXIII. Fundamentals of Nuclear Star Clusters over Seven Decades in Galaxy Mass

Rubén Sánchez-Janssen[1,2], Patrick Côté[2], Laura Ferrarese[2,3], Eric W. Peng[4,5], Joel Roediger[2], John P. Blakeslee[2], Eric Emsellem[6,7], Thomas H. Puzia[8], Chelsea Spengler[2], James Taylor[9], Karla A. Álamo-Martínez[8], Alessandro Boselli[10], Michele Cantiello[11], Jean-Charles Cuillandre[12], Pierre-Alain Duc[13,14], Patrick Durrell[15], Stephen Gwyn[2], Lauren A. MacArthur[16], Ariane Lançon[13], Sungsoon Lim[4,5], Chengze Liu[17], Simona Mei[18,19,20], Bryan Miller[21], Roberto Muñoz[8], J. Christopher Mihos[22], Sanjaya Paudel[23], Mathieu Powalka[13], and Elisa Toloba[24]

[1] STFC UK Astronomy Technology Centre, Royal Observatory, Blackford Hill, Edinburgh, EH9 3HJ, UK; ruben.sanchez-janssen@stfc.ac.uk
[2] NRC Herzberg Astronomy and Astrophysics, 5071 West Saanich Road, Victoria, BC, V9E 2E7, Canada
[3] Gemini Observatory, Northern Operations Center, 670 N. A'ohoku Place, Hilo, HI 96720, USA
[4] Department of Astronomy, Peking University, Beijing 100871, People's Republic of China
[5] Kavli Institute for Astronomy and Astrophysics, Peking University, Beijing 100871, People's Republic of China
[6] European Southern Observatory, Karl-Schwarzschild-Str. 2, D-85748 Garching, Germany
[7] Centre de Recherche Astrophysique de Lyon and École Normale Supérieure de Lyon, Observatoire de Lyon, Université Lyon 1, 9 avenue Charles André, F-69230 Saint-Genis Laval, France
[8] Institute of Astrophysics, Pontificia Universidad Católica de Chile, Av. Vicuña Mackenna 4860, 7820436 Macul, Santiago, Chile
[9] Department of Physics and Astronomy, University of Waterloo, Waterloo, ON N2L 3G1, Canada
[10] Laboratoire d'Astrophysique de Marseille—LAM, Université d'Aix-Marseille & CNRS, UMR7326, 38 rue F. Joliot-Curie, F-13388, Marseille Cedex 13, France
[11] INAF-Osservatorio Astronomico di Teramo, Italy
[12] Canada–France–Hawaii Telescope Corporation, Kamuela, HI 96743, USA
[13] Observatoire Astronomique, Université de Strasbourg & CNRS UMR 7550, 11 rue de l'Université, F-67000 Strasbourg, France
[14] AIM Paris Saclay, CNRS/INSU, CEA/Irfu, Université Paris Diderot, Orme des Merisiers, F-91191 Gif sur Yvette Cedex, France
[15] Department of Physics and Astronomy, Youngstown State University, One University Plaza, Youngstown, OH 44555, USA
[16] Department of Astrophysical Sciences, Princeton University, Princeton, NJ 08544, USA
[17] Center for Astronomy and Astrophysics, Department of Physics and Astronomy, Shanghai Jiao Tong University, Shanghai 200240, People's Republic of China
[18] LERMA, Observatoire de Paris, PSL Research University, CNRS, Sorbonne Universités, UPMC Univ. Paris 06, F-75014 Paris, France
[19] University of Paris Denis Diderot, University of Paris Sorbonne Cité (PSC), F-75205 Paris Cedex 13, France
[20] Jet Propulsion Laboratory, Cahill Center for Astronomy & Astrophysics, California Institute of Technology, 4800 Oak Grove Drive, Pasadena, California, USA
[21] Gemini Observatory, Casilla 603, La Serena, Chile
[22] Department of Astronomy, Case Western Reserve University, Cleveland, OH, USA
[23] Korea Astronomy and Space Science Institute, Daejeon 305-348, Republic of Korea
[24] Department of Physics, University of the Pacific, 3601 Pacific Avenue, Stockton, CA 95211, USA

Received 2017 October 23; revised 2018 November 28; accepted 2018 November 28; published 2019 June 7

Abstract

Using deep, high-resolution optical imaging from the Next Generation Virgo Cluster Survey, we study the properties of nuclear star clusters (NSCs) in a sample of nearly 400 quiescent galaxies in the core of Virgo with stellar masses $10^5 \lesssim M_*/M_\odot \lesssim 10^{12}$. The nucleation fraction reaches a peak value $f_n \approx 90\%$ for $M_* \approx 10^9\,M_\odot$ galaxies and declines for both higher and lower masses, but nuclei populate galaxies as small as $M_* \approx 5 \times 10^5\,M_\odot$. Comparison with literature data for nearby groups and clusters shows that at the low-mass end nucleation is more frequent in denser environments. The NSC mass function peaks at $M_{\rm NSC} \approx 7 \times 10^5\,M_\odot$, a factor 3–4 times larger than the turnover mass for globular clusters (GCs). We find a nonlinear relation between the stellar masses of NSCs and those of their host galaxies, with a mean nucleus-to-galaxy mass ratio that drops to $M_{\rm NSC}/M_\star \approx 3.6 \times 10^{-3}$ for $M_* \approx 5 \times 10^9\,M_\odot$ galaxies. Nuclei in both more and less massive galaxies are much more prominent: $M_{\rm NSC} \propto M_*^{0.46}$ at the low-mass end, where nuclei are nearly 50% as massive as their hosts. We measure an intrinsic scatter in NSC masses at a fixed galaxy stellar mass of 0.4 dex, which we interpret as evidence that the process of NSC growth is significantly stochastic. At low galaxy masses we find a close connection between NSCs and GC systems, including very similar occupation distributions and comparable total masses. We discuss these results in the context of current dissipative and dissipationless models of NSC formation.

Key words: galaxies: clusters: individual (Virgo) – galaxies: dwarf – galaxies: nuclei – galaxies: photometry – galaxies: star clusters: general – globular clusters: general

1. Introduction

The very central regions of galaxies are extreme astrophysical environments, sites where numerous complex mechanisms operate simultaneously. They mark the bottom of the galactic potential well, where matter has been accumulating throughout the entire galactic history. A fraction of their constituent material can be traced back to the earliest generations of stars that formed during the rapid collapse of the rarest density peaks (Diemand et al. 2005), but also to more recent epochs as a product of recurrent gas inflows followed by associated star formation events. As a result, these inner regions feature the highest galactic stellar densities and the shortest relaxation times, and it is no accident that they also harbor the two types of known compact massive objects (CMOs), namely massive black holes (MBHs) and nuclear star clusters (NSCs).

NSCs are compact stellar systems with half-light radii in the range of 1–50 pc and stellar masses stretching from as low as $10^4\,M_\odot$ to as high as $10^8\,M_\odot$. On average, they tend to be larger and more massive than the typical globular cluster (GC), but remarkably, their central stellar surface densities can be even more extreme—among the highest known, sometimes exceeding $\Sigma_c = 10^5\,M_\odot\,\mathrm{pc}^{-2}$ (e.g., Lauer et al. 1998; Hopkins et al. 2009). These central stellar densities are only rivaled by those of some GCs and ultracompact dwarfs (UCDs; Hilker et al. 1999; Drinkwater et al. 2000). UCDs also present remarkable similarities with NSCs in terms of stellar population content (Chilingarian et al. 2008; Norris et al. 2014; Liu et al. 2015a). All this, combined with the fact that UCDs tend to live in close proximity to massive galaxies (Haşegan et al. 2005; Hau et al. 2009; Liu et al. 2015a) and as a population have distinct kinematical properties from galactic GC systems (GCSs; Zhang et al. 2015), has led to the suggestion that a non-negligible fraction of UCDs may represent the remnants of tidally disrupted nucleated galaxies (Drinkwater et al. 2003; Pfeffer & Baumgardt 2013, but see Mieske et al. 2006 and De Propris et al. 2005 for arguments against this scenario). The discovery (Seth et al. 2014; Ahn et al. 2017) that M60-UCD 1 in the Virgo cluster harbors an MBH contributing ≈15% of the total mass lends further support to the nuclear origin of (at least) the most massive UCDs. The threshing scenario has also been put forward to explain the chemical, structural, and dynamical anomalies of the most massive GCs in the Local Group, like ωCen in the Galaxy (Lee et al. 1999; Hilker & Richtler 2000; Bekki & Freeman 2003) and Mayall II/G1 in M31 (Meylan et al. 2001; Bekki & Chiba 2004; Ma et al. 2007).

NSCs inhabit galaxies spanning a wide range of masses, morphological types, and gas content, and nucleation seems to be a complex function of all these parameters (Binggeli et al. 1987; Binggeli & Cameron 1991; Carollo et al. 1998; Böker et al. 2002; Walcher et al. 2005; Cote et al. 2006, 2007; Seth et al. 2006; Lisker et al. 2007; Georgiev et al. 2009; Glass et al. 2011; Turner et al. 2012; den Brok et al. 2014; Georgiev & Böker 2014). Interestingly, galaxies and NSCs display a variety of scaling relations, including with their stellar masses (e.g., Scott & Graham 2013; Georgiev et al. 2016) and their stellar populations or colors (Walcher et al. 2005; Turner et al. 2012; Georgiev & Böker 2014). This suggests that their formation is intricately linked to that of their host galaxy. And perhaps it is not entirely surprising that some of these scaling relations may be similar to those followed by MBHs, a picture that further relates the two families of CMOs (Ferrarese et al. 2006a; Wehner & Harris 2006; Graham & Spitler 2009).

Formation scenarios for NSCs can be broadly divided into two categories. The first one involves a dissipationless process, whereby the orbits of pre-existing dense star clusters decay as a result of dynamical friction and produce mergers in the central regions of the galaxy (Tremaine et al. 1975; Capuzzo-Dolcetta 1993; Capuzzo-Dolcetta & Miocchi 2008a, 2008b; Agarwal & Milosavljević 2011; Arca-Sedda & Capuzzo-Dolcetta 2014; Gnedin et al. 2014). The second scenario consists of a dissipative mode through in situ central star formation driven by gas inflows and condensation (Bekki et al. 2006; Bekki 2007; Antonini et al. 2015), with the first seeds developing perhaps as early as the epoch of reionization (Cen 2001). The latter growth mechanism is of course regulated by the availability of sufficient gas reservoirs in the central regions and internal feedback mechanisms. Most likely both processes contribute to some degree to the formation of the NSCs we observe in the Local Universe (Hartmann et al. 2011; Antonini et al. 2015), and hybrid scenarios involving the coalescence of gas-rich star clusters have been proposed (Guillard et al. 2016). The heterogeneity of the proposed formation scenarios is consistent with observations of the stellar populations in NSCs. They tend to be rather complex, showing evidence of multiple generations of stars and younger mean ages and higher metallicities than typical in GCs (Rossa et al. 2006; Walcher et al. 2006; Puzia & Sharina 2008; Paudel et al. 2011). But the relative weight of the different formation mechanisms and how this breakdown depends on host galaxy properties are unknown. Related and perhaps more fundamental questions are what determines whether a galaxy forms an NSC in the first place and what mechanisms regulate its subsequent growth.

Considering all the unknowns about the origin and growth of NSCs, it is fundamental to accurately characterize their occurrence and how they relate to their host galaxies. In this contribution we take a step forward in this direction and present a comprehensive study on the abundance and properties of NSCs in a volume- and mass-limited sample of galaxies in the Virgo cluster spanning seven decades in stellar mass. Focusing our study on cluster galaxies presents several advantages. First, the high densities in clusters directly translate into large galaxy samples and into studies with significant statistical power. Second, it is also straightforward to translate abundance results into volume-limited quantities—and this is a much harder exercise in the field. Finally, because all these galaxies share a common (overdense) environment, statistically speaking they first collapsed at similarly early epochs and have been subject to roughly the same amount of environmental effects. In the particular case of quiescent galaxies in the cores of clusters as massive as Virgo, star formation activity is expected to have ceased at least 5–6 billion years ago (e.g., Mistani et al. 2015). The lack of substantial star formation activity in the recent past for these red-sequence cluster galaxies implies that their NSCs should have been polluted to a lesser degree than those at the centers of gas-rich, more luminous disk galaxies—but our knowledge about the stellar populations of faint NSCs is still limited (Spengler et al. 2017; Ordenes-Briceño et al. 2018). Readers interested in the properties of NSCs in those star-forming systems are referred to recent works by Georgiev & Böker (2014), Carson et al. (2015), and Georgiev et al. (2016). Georgiev et al. (2009) present a study on the nuclei of lower-mass dwarf irregulars.

This paper is organized as follows. Section 2 describes the methods for NSC detection and the measurement of NSC properties in the Next Generation Virgo Cluster Survey (NGVS) images. In Section 3 we study the nucleation fraction in the core of the Virgo cluster, followed by an investigation of the scaling relations between NSCs and their host galaxies in Section 4. Section 5 presents a discussion on the previous results in the context of NSC formation models and on the relationship to other star cluster systems. Finally, in Section 6 we summarize the main findings of this work and lay out our conclusions. Throughout this manuscript we use a common distance modulus $(m - M) = 31.09$ mag for all candidate Virgo members, corresponding to the mean distance of $D = 16.5$ Mpc to the Virgo cluster derived

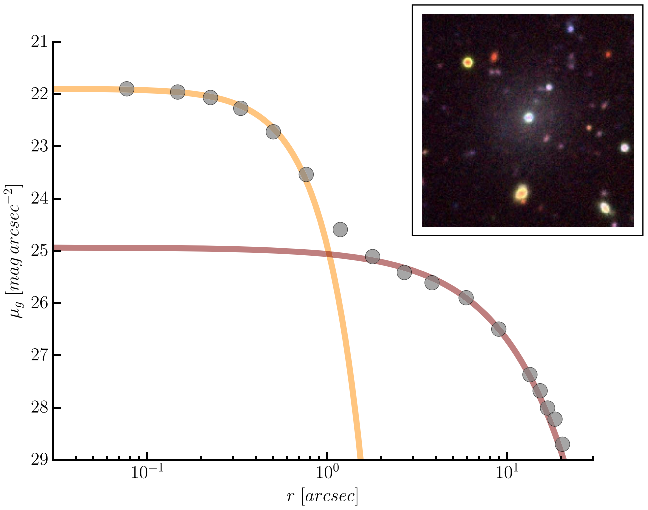

Figure 1. Structural characterization of the nucleated low-mass galaxy VCC 1070 in the NGVS. The gray points show the surface brightness profile as measured by ELLIPSE. The maroon and orange lines correspond to the seeing-convolved best-fit Sérsic profiles to the galaxy and NSC components, respectively. The inset image shows a *gri* composite of the galaxy. Note the remarkable prominence of the NSC in VCC 1070.

through the surface brightness fluctuations method (Mei et al. 2007; Blakeslee et al. 2009). This translates into a physical scale of 80 pc arcsec^{-1}.

2. Detection and Characterization of NSCs in the NGVS

Detailed descriptions of the NGVS and its associated data products are given elsewhere (Ferrarese et al. 2012, 2016). Briefly, here we only use data on the core of Virgo, which for our purposes refers to the square region roughly centered on M87 and $2° = 0.58$ Mpc $= 0.37\,R_{\rm vir}$ on the side. This area was imaged in the $u'griz'K_s$ bandpasses, and galaxies were detected using a ring median filter algorithm optimized to extract low surface brightness objects. Virgo members were then identified using a combination of colors and structural and quantitative morphological parameters, which were further complemented with a visual inspection by several members of our team. This process resulted in a parent sample of 404 galaxies in the core of Virgo spanning approximately seven decades in stellar mass, $10^5 \lesssim M_*/M_\odot \lesssim 10^{12}$ (Ferrarese et al. 2016). In this study we are only interested in the NSCs of quiescent galaxies, and we accordingly discard 24 objects that have evidence of ongoing star formation activity (see Roediger et al. 2017).

The structural characterization of these galaxies is presented in full in L. Ferrarese et al. (2019). Here we only provide the most salient details pertaining to the analysis of NSCs. A full isophotal analysis is carried out using a semi-automated code that (i) extracts image cutouts and masks contaminants and cosmetics; (ii) performs isophotal fitting and extracts one-dimensional profiles for the surface brightness, ellipticity, major-axis position angle, isophotal center, and deviations of the isophotes from pure ellipses; and (iii) carries out parametric fits to the surface brightness profiles while accounting for the effects of the point-spread function (PSF; see Figure 1). The galaxy body is modeled with a single Sérsic (1968) function, which provides an adequate description of these smooth, nearly oblate galaxies (Sánchez-Janssen et al. 2016). If necessary, a central nuclear component is included in the fits. NSCs are also modeled with Sérsic functions, but with a few exceptions these nuclei remain unresolved despite the exquisite image quality of the NGVS (PSF FWHM ≈ 0.6 arcsec in the *i*-band). All the quoted errors correspond to the 1σ formal uncertainty of the fitted Sérsic profiles. The analysis is carried out independently in each of the photometric bands.

The detection of barely resolved or unresolved NSCs is always challenging. The operational definition of NSCs in this paper requires the existence of a luminosity excess above the main stellar distribution in the core regions of the galaxies. The identification of such objects is based on the relative quality of the Sérsic and double Sérsic fits (as measured by the fit χ^2), complemented by a visual inspection of color and unsharp-masked images of the galaxies. In the Virgo core we classify 107 galaxies as nucleated. The formal limiting magnitude for unresolved sources in the NGVS is $g = 25.9$ mag (Ferrarese et al. 2012), and this translates into a limiting mass for NSCs $\log(M_{\rm NSC}/M_\odot) \approx 4.5$. However, because the nuclei are additionally visually classified, the effective detection threshold in this study may be slightly higher (see details in Section 4.2.1).

Stellar masses for the galaxies and the NSCs are obtained through modeling of their spectral energy distributions (SEDs) in the $u'griz'$ bands. Details will be presented in J. Roediger et al. (2018, in preparation), but essentially we employ the Flexible Stellar Population Synthesis models of Conroy et al. (2009), assuming exponentially declining star formation histories and a Chabrier initial mass function. The SEDs are fit to a grid of 50,000 synthetic models with metallicities in the $0.01 \leqslant Z/Z_\odot \leqslant 1.6$ range, star formation timescales $0.5 \leqslant \tau \leqslant 100\,{\rm Gyr}^{-1}$, and luminosity-weighted ages between 5 and 13 Gyr. In this work we carry out several comparisons between the NGVS data and other samples from the literature for which multiwavelength photometry is not always available. Thus, for the literature samples we convert the luminosities to masses using the M_*/L ratios derived from the above SED fitting procedure. Specifically, for galaxies we use the median relation between the M_*/L ratios as a function of luminosity in the corresponding band (usually g or i) so that we account for mass-dependent variations. For NSCs we simply use the median M_*/L from our sample of nuclei. Typical uncertainties for these stellar masses are $\sigma(\log M_*) \approx 0.15$ dex and $\sigma(\log M_{\rm NSC}) \approx 0.20$ dex. The photometric properties of galaxies and NSCs in the core of Virgo are presented in Table 4 and Table 5, respectively.

Because faint NSCs are unresolved and hard to distinguish from stars, we quantify the likelihood of contamination by chance superposition of galactic stellar interlopers over the geometric center of a galaxy as follows. We first compute the density of stars in the Virgo core, $\rho_\star$, using a catalog of largely unresolved sources brighter than $g = 25$ mag (0.2 mag fainter than the faintest NSC in the sample). These sources are assigned probabilities of being either stars, GCs, or background galaxies using a mixture model algorithm that incorporates information about their SED and structure (E. W. Peng et al. 2018, in preparation). From that catalog we only select the ≈5500 sources with $P({\rm star}) > 0.5$ that have colors $0.5 < (g{-}i) < 1.15$, which is roughly the range expected for NSCs and UCDs (see Liu et al. 2015a and Figure 3). We further assume a maximum nucleus–galaxy offset of $R = 2$ arcsec (equivalent to 160 pc), which is the maximum distance found by Cote et al. (2006) in their analysis of ACSVCS nuclei. In our case the great majority of nuclei are found within 0.4 arcsec of the galaxy center (L. Ferrarese et al. 2019). Using these numbers we estimate a total number of $\rho_\star \pi R^2 \approx 1.5 \times 10^{-3}$ stars per galaxy. Equivalently, this implies

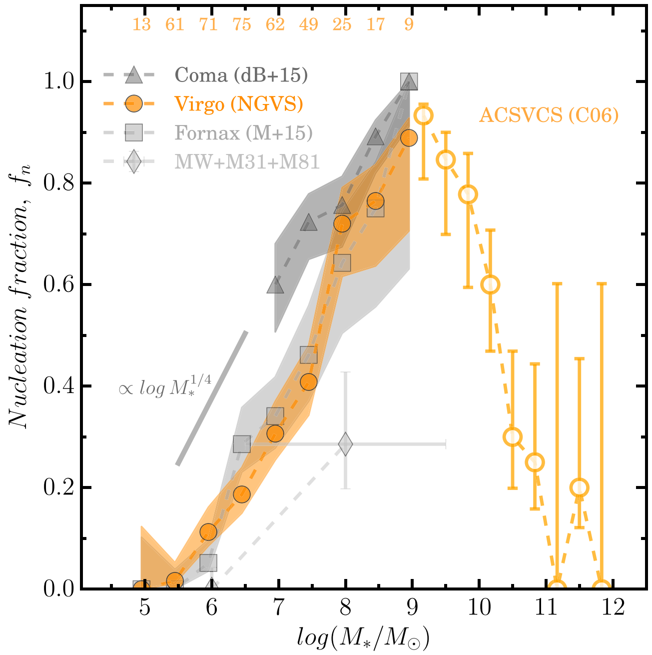

Figure 2. Fraction of nucleated galaxies in different environments as a function of galaxy stellar mass. The Virgo, Fornax, and Coma clusters are represented with circles, squares, and triangles, respectively. The two diamond symbols correspond to the satellites of three nearby spiral-dominated galaxy groups. Shaded regions and error bars indicate the corresponding 68% Bayesian credible interval, and the figures at the top show the total number of NGVS galaxies in each stellar mass bin. Note how, at fixed stellar mass, the fraction of nucleated galaxies in Virgo is always lower than that in Coma. The rapid decline toward low masses implies that the faintest nucleated low-mass galaxy in Virgo has a stellar mass $M_* \approx 5 \times 10^5\,M_\odot$.

that in this worst-case scenario no more than one galaxy in the Virgo core would be affected by a star being close enough to its center to be mistaken for an NSC.

3. Nucleation Fraction

We first turn our attention to the occurrence of NSCs in the core of Virgo. In Figure 2 we show with solid circles f_n, the fraction of nucleated galaxies in the NGVS as a function of galaxy stellar mass for objects with masses $M_* \leqslant 10^9\,M_\odot$. The number of galaxies in the Virgo core area more massive than this limit drops quickly, as indicated by the numbers at the top of Figure 2. This results in too uncertain estimates of the nucleation fraction for more luminous galaxies. For completeness, in the $10^9 < M_*/M_\odot < 10^{12}$ mass range we derive the fraction of nucleated galaxies in Virgo from the ACSVCS (Cote et al. 2006), which is not limited to the core region and therefore has stronger statistical power at the high-mass end. Throughout this paper, and unless otherwise stated, all uncertainties associated with binomial proportions correspond to the 68% Bayesian credible interval.

Consistent with previous work we find that the nucleation fraction is very high at intermediate masses, such that at $M_* \approx 10^9\,M_\odot$ over 90% of the galaxies in the core of Virgo harbor an NSC. The nucleation fraction was found by Cote et al. (2006) to drop sharply for massive galaxies, a behavior that is often attributed to the highly disruptive power of the MBHs that inhabit the central regions of these galaxies (see Antonini 2013 and Section 5). Interestingly, we find that f_n also decreases toward lower masses, albeit at a slightly slower rate, so that the NSC occupation distribution almost resembles a lognormal function. At low masses this decline is well described by $f_n \propto \log M_*^{1/4}$. We identify a threshold value below which no low-mass galaxy with $\langle\mu_g\rangle_e < 28\,\mathrm{mag\,arcsec^{-2}}$ in the core of Virgo is nucleated, $M_* \approx 5 \times 10^5\,M_\odot$ (see Figure 2). This indicates that either NSC formation is highly inefficient in low-mass halos or, alternatively, some mechanism enhances NSC disruption in these shallow potentials. The strong dependence of the nucleation fraction on galaxy mass also implies that care must be taken when comparing different samples if they span different mass ranges. The *global* nucleation fraction is an ill-defined quantity, unless the mass range under study is specified.

In Figure 2 we also explore the dependence of the nucleation fraction on the global environment, that is, the mass of the host potential where the galaxies reside. We include data on the fraction of early-type nucleated galaxies in the Coma (den Brok et al. 2014) and Fornax clusters (Muñoz et al. 2015) as well as in three spiral-dominated groups in the Local Universe, namely the Milky Way (MW), M31, and M81. For these two data sets we use the published *i*-band magnitudes and luminosity-dependent mass-to-light ratios, which vary nonlinearly in the range $0.5 < M_*/L_i < 1.7$ (see Zhang et al. 2017). For the NSCs we use the median $M_*/L_i = 1.3$ from our sample of Virgo nuclei. Details of the methodology used to identify nucleated galaxies in the nearby groups and to estimate their stellar masses are provided in the Appendix. It is also important to remark that the effective spatial resolutions are almost identical for the different cluster samples, because the larger distance of Coma is compensated by the use of *Hubble Space Telescope* (*HST*)/Advanced Camera for Surveys (ACS) imaging. We thus sample a wide range of host halo masses, from $M_h \approx 10^{15}\,M_\odot$ for Coma to $M_h \approx 10^{14}\,M_\odot$ for Virgo and Fornax to $M_h \approx 10^{12}\,M_\odot$ for the three groups with L^* centrals. We note that the three cluster samples only include galaxies from roughly the same physical regions, 0.2–0.25 R_{vir}, and so can be directly compared.

We find that in all environments the nucleation fraction is a similarly strong function of galaxy stellar mass, but we unveil a secondary dependence on host halo mass: at fixed M_* the fraction of galaxies harboring NSCs is larger in denser environments. While the f_n curves in Virgo and Fornax display almost identical behavior, at all stellar masses the nucleation fraction is systematically larger in Coma and smaller in the nearby groups. The effect is perhaps best appreciated by comparing the integrated nucleation fraction within the common $[10^7, 10^9]\,M_\odot$ mass range, where 77%, 53%, and 56% of the galaxies host an NSC in Coma, Virgo, and Fornax, respectively. The figure for the three spiral-dominated groups combined drops to 29%, but it is necessarily a noisier measurement due to the reduced satellite sample size (only 14 galaxies in this mass range). It would be interesting to explore to which extent the high nucleation fraction in massive clusters like Coma holds toward lower stellar masses, i.e., whether the threshold mass for NSC occurrence we find in Virgo is roughly universal or also varies with host halo mass. We conclude that while stellar mass is the main parameter governing NSC occurrence, NSC abundance is also enhanced in high-density environments.

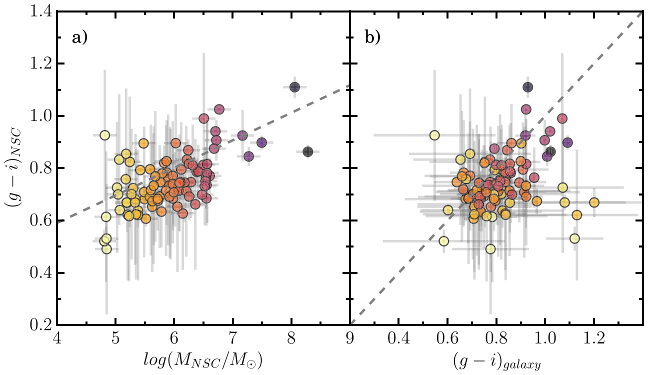

Figure 3. Colors of NSCs in the core of the Virgo cluster. Left: The $(g-i)$ colors of the NSCs are shown against the mass of the nucleus. The two quantities are correlated, and the dashed line shows the best-fit relation. Right: The colors are now plotted against the color of the host galaxy. The correlation is much weaker. In both panels the symbols are color-coded according to $M_{\rm NSC}$.

4. Scaling Relations between NSCs and Their Host Galaxies

Having established the frequency with which NSCs occur in Virgo galaxies, we explore their colors, their masses, and the relation to the properties of their host galaxies.

4.1. Colors of NSCs

In Figure 3(a) we show the relation between NSC masses and NSC $(g-i)$ colors for the galaxies in the core of Virgo. We note that this is a slightly reduced subsample where we have excluded 12 objects that have highly uncertain $(g-i)$ colors ($\sigma_c > 0.3$ mag). Consistent with previous work (e.g., Turner et al. 2012) we find that the colors of NSCs correlate with $M_{\rm NSC}$, such that more massive nuclei tend to be slightly redder (Pearson's correlation coefficient $r = 0.6$). The dashed line in this panel shows the best-fit relation, $(g-i) = 0.17 + 0.1 \log M_{\rm NSC}$. The median color for the sample is $(g-i) = 0.73$, which as shown by Roediger et al. (2017) is remarkably consistent with the peak of the galaxy color distribution at low masses. In the right panel, Figure 3(b) shows the same colors now plotted against the colors of the host galaxies. The dashed line indicates the identity relation. The two quantities are only weakly correlated ($r = 0.23$), and we consider this to be an indication that the connection is only a secondary effect. As we will show in the next section, less massive galaxies (which are bluer) tend to have less massive NSCs. And because the mass of an NSC is correlated with its color, we naturally find marginally bluer nuclei in bluer galaxies. The mean color difference is only $\langle\Delta(g-i)\rangle = \langle(g-i)_{\rm galaxy} - (g-i)_{\rm NSC}\rangle = 0.06$, which indicates that NSCs have marginally bluer colors than their host galaxies. This is confirmed upon inspection of the fraction of NSCs that have $\langle\Delta(g-i)\rangle > 0$, which amounts to 75%. This is in agreement with previous work (Paudel et al. 2011), indicating that NSCs may be marginally younger and/or more metal-poor than the bulk of stars in the galactic body. A more detailed analysis of the SEDs and the stellar population content of NSCs using NGVS data is presented in Spengler et al. (2017).

4.2. Relation to the Host Galaxy

4.2.1. The NSC-to-galaxy Mass Relation

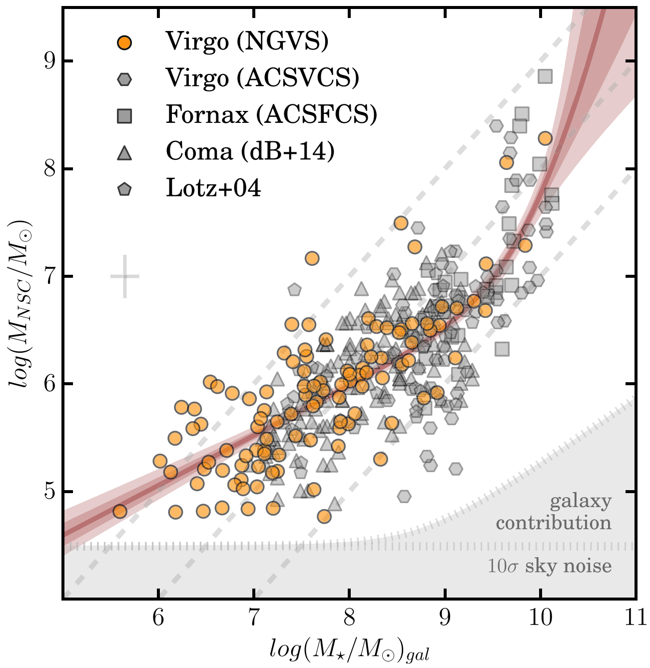

Figure 4. NSC-to-galaxy mass relation. The NGVS data for the core region are represented with circles, but here we also include literature data for early-type galaxies in Virgo, Fornax, and Coma (see text for details). The error bar shows the typical uncertainty in the mass estimates. The shaded region at the bottom indicates the NSC mass equivalent to the 10σ detection limit in the NGVS, including the contribution of the underlying galaxy light. The three dashed lines, from right to left, correspond to constant NSC mass fractions of 0.1%, 1%, and 10%. Note that while more massive galaxies harbor more massive nuclei, the relation is nonlinear. The best-fit relation is plotted as a solid line together with the 68% and 95% confidence intervals. We measure an intrinsic scatter for the relation of nearly 0.4 dex, which we interpret as evidence of stochastic NSC growth.

In Figure 4 we show the relation between the stellar masses of the NSCs and those of their host galaxies. The NGVS data for the core region are represented with circles, but here we also include data for other early-type galaxies in Virgo (from the ACSVCS; Cote et al. 2004), Fornax (ACSFCS; Turner et al. 2012), Coma (den Brok et al. 2014), and the sample of Virgo and Fornax faint dEs from Lotz et al. (2004). The three dashed lines, from right to left, correspond to constant NSC mass fractions of 0.1%, 1%, and 10%. The shaded region at the bottom of the panel indicates the NSC mass equivalent to the 10σ detection limit for unresolved sources in the NGVS, $\log(M_{\rm NSC}/M_\odot) \approx 4.5$ (see Ferrarese et al. 2012). Two sources contribute to the local background against which NSCs are detected, namely the underlying galaxy stellar light and the sky brightness. Here the galaxy term is estimated by computing the Poisson noise associated with the average galaxy central surface brightness as a function of stellar mass. It is only dominant for relatively massive galaxies, $\log(M_{\rm NSC}/M_\odot) \gtrsim 8.5$, whereas the sky brightness is the main source of noise for fainter systems. We note that our effective detection threshold may be slightly higher than shown. NSCs are additionally visually classified, and it is possible that in this process we have discarded extremely faint nuclei that may fall below the detection limit in a single band (therefore giving them a questionable visual appearance).

An important conclusion that can be readily drawn from Figure 4 is that, contrary to what we have found regarding the nucleation fraction, the NSC-to-galaxy stellar mass relation for early-type cluster galaxies seems to be independent of environment. All galaxies in Virgo, Fornax, and Coma exhibit

Table 1
Bayesian Fit to the NSC-to-galaxy Stellar Mass Relation

Parameter	Prior	Posterior
$\log(M'_{\rm NSC}/M_\odot)$	[5.0, 9.0]	$7.29^{+0.11}_{-0.13}$
$\log(M'_*/M_\odot)$	[6.0, 11.0]	$9.73^{+0.10}_{-0.12}$
β	[0.0, 10.0]	$0.46^{+0.03}_{-0.04}$
δ	[0.0, 10.0]	$0.43^{+0.23}_{-0.17}$
$\ln V$	[−5.0, 2.0]	$-1.83^{+0.09}_{-0.09}$

Note. The priors for the parameters listed above are assumed to be uniform within the closed intervals shown in the second column. The posterior figures correspond to the median of the marginalized posterior distribution and the associated 68% confidence interval.

the same behavior, albeit with large intrinsic scatter. The universality of the NSC-to-galaxy stellar mass relation suggests that the mass of an NSC is primarily controlled by the galaxy mass, but its large intrinsic scatter indicates that the process of mass deposition in the nuclear region is probably quite stochastic in nature (see discussion below). It is also evident that even though more massive galaxies host the most massive nuclei, the relation is nonlinear, featuring significant steepening at the massive end. The shape of the relation is very reminiscent of the stellar-to-halo mass relation (SHMR), so we provide a quantitative description using the following five-parameter functional form:

$$\log M_{\rm NSC} = \log M'_{\rm NSC} - \frac{1}{2} + \beta \log\left(\frac{M_*}{M'_*}\right) + \frac{\left(\frac{M_*}{M'_*}\right)^{\delta}}{1 + \left(\frac{M_*}{M'_*}\right)^{-\gamma}}, \qquad (1)$$

where $M'_{\rm NSC}$ is a characteristic NSC mass, M'_* is a characteristic galaxy stellar mass, β is the slope of the relation at the low-mass end, and δ and γ determine the massive end slope. This expression has been shown to provide an adequate description of the SHMR in all environments and at all redshifts (see Behroozi et al. 2013; Grossauer et al. 2015) and will help us better interpret our results on NSC properties in the larger context of galaxy formation in a γ cold dark matter (CDM) framework.

We carry out a Bayesian fit to Equation (1) while simultaneously allowing for intrinsic scatter at a fixed galaxy stellar mass, parameterized by a variance V. Because of the universality of the $M_{\rm NSC}$–M_* relation, and unless otherwise stated, we perform the analysis on the combined data set shown in Figure 4. We have verified that fitting only the NGVS data does not modify the results. We assume uniform priors for the parameters in closed intervals as indicated in Table 1, and we keep $\gamma = 1$ because it is largely unconstrained by the data, due to the small sample size at high masses (see also Grossauer et al. 2015).

The last column of Table 1 shows the median and 68% confidence interval for the marginalized posterior distributions of the parameters. The corresponding best-fit relation is plotted as a solid line in Figure 4, together with the 68% and 95% confidence intervals. According to this fit, NSC masses scale as $M_{\rm NSC} \propto M_*{}^{0.46}$ at the low-mass end, a behavior that extends for over four decades in galaxy stellar mass. This is a shallower slope than what was found by den Brok et al. (2014) in Coma, $\beta = 0.57 \pm 0.05$, and by Scott & Graham (2013) using a compilation from literature data, $\beta = 0.6 \pm 0.1$.

The NSC-to-galaxy stellar mass relation features a characteristic mass for nuclei $M'_{\rm NSC} \approx 2 \times 10^7\, M_\odot$ in galaxies with stellar masses $M'_* \approx 5 \times 10^9\, M_\odot$. The ratio $(M'_{\rm NSC}/M'_*) \approx 3.6 \times 10^{-3}$ that we infer is in perfect agreement with the mean NSC mass fraction obtained in the ACSVCS and ACSFCS studies (Cote et al. 2006; Turner et al. 2012), which can be simply explained by their sample being dominated in number by intermediate-mass cluster galaxies. We also measure an intrinsic scatter at a fixed galaxy stellar mass of $\sqrt{V} = 0.4$ dex, which is consistent with the value of ≈0.36 dex measured by den Brok et al. (2014) in Coma. The value of V is anticorrelated with the estimated uncertainties in the measurements of $M_{\rm NSC}$, such that if the uncertainties are underestimated, then V will be smaller. We interpret this large intrinsic scatter as indication that the process of NSC growth is quite stochastic (see Section 5), and note that high stochasticity is a general characteristic of star formation processes in all low-mass halos (Ricotti et al. 2016).

4.2.2. Relation to Galaxy Structure

There are previous claims in the literature that nucleation and the properties of NSCs are related to galaxy structure. For example, den Brok et al. (2014) found that at a fixed galaxy luminosity, galaxies tend to have more luminous clusters when they have higher Sérsic indices and rounder shapes. The relation between galaxy structure and nucleation will be explored in detail in a different paper of this series (P. Côté et al. 2018, in preparation). Here we only point out that there is a tendency for nucleated galaxies to have slightly smaller effective radii at a fixed galaxy luminosity, but the trend is not statistically significant considering the small sample size. We will address this question in detail once the full NGVS sample is available.

4.3. The NSC Mass Function in Virgo

The histogram in Figure 5 shows the NSC mass function (NSCMF) in the core of Virgo. The solid line with circles shows the best-fit Gaussian function with parameters $\mu = 5.82$ dex and $\sigma = 0.68$. This functional form is selected for historical reasons and to facilitate a direct comparison with previous work on other compact stellar systems, such as GCs and UCDs. As already noted by Turner et al. (2012), the observed distribution is nothing but the convolution of the nucleation fraction with the nucleus-to-galaxy mass relation, and there is no obvious physical reason for this quantity to be normally distributed. The shaded vertical region in Figure 5 indicates our 10σ detection limit of $\log(M_{\rm NSC}/M_\odot) = 4.5$ (see Section 4.2.1). The sharp cutoff of the NSCMF at low masses suggests that we may be missing a small fraction of the nuclei below this mass limit, but the declining nucleation fraction toward low masses leads us to the conclusion that it has to be a very small number.

We compare the NSCMF in the NGVS with that derived from the den Brok et al. (2014) data set for Coma early-type

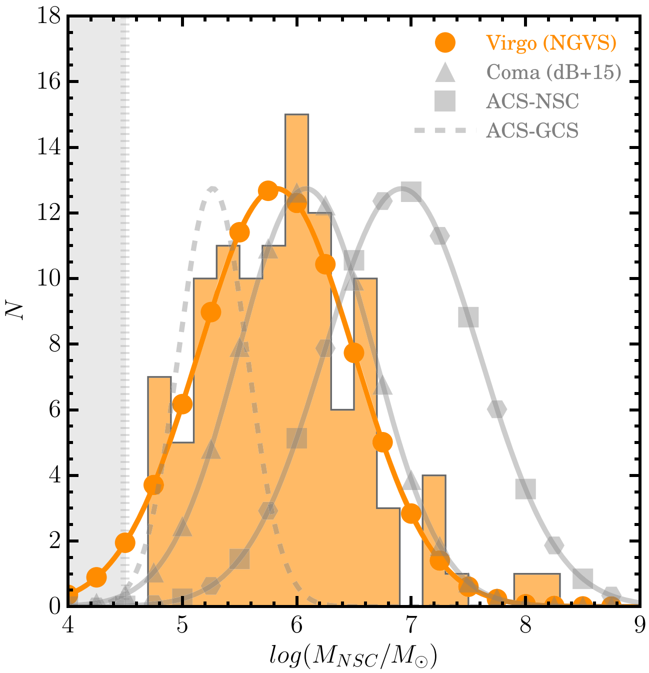

Figure 5. The NSCMF in the core of Virgo is shown here with a filled histogram. The best-fit Gaussian function is also plotted with circles, as well as the mass functions for other samples of NSCs and GCs from the literature. For reference, the typical NSC in Virgo is nearly four times as massive as the typical GC. The shaded vertical region indicates our 10σ detection limit for NSCs.

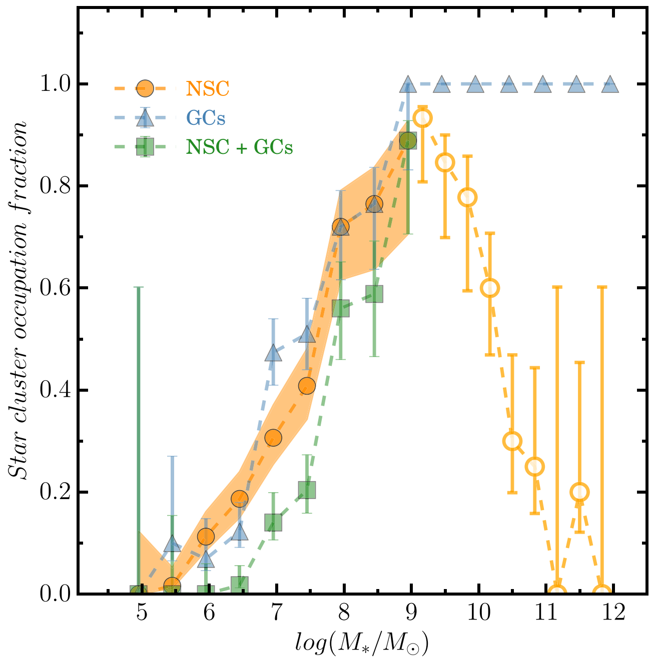

Figure 6. Star cluster occupation distribution in the core of Virgo as a function of galaxy stellar mass. The fractions of galaxies hosting an NSC, GCs, and the two types of clusters simultaneously are represented with circles, triangles, and squares, respectively. Shaded regions and error bars indicate the corresponding 68% Bayesian credible interval. The remarkable similarity between these occupation distributions indicates a close connection between the different families of compact stellar systems.

galaxies (triangle line). We transform their *i*-band magnitudes to stellar masses and obtain the best-fit Gaussian parameters $\mu = 6.08$ and $\sigma = 0.59$. Thus, the Coma NSCMF is very similar to ours, but it features a slightly more massive turnover mass, which we attribute to the brighter cutoff in the Coma galaxy sample ($M_i \leqslant -14$ mag). We also compare with the combined samples from the Virgo and Fornax ACS surveys (Turner et al. 2012; square–hexagon line). The bias is even more acute for these samples, which provide a very uniform sampling of the massive end of the NSCMF but lack galaxies fainter than $M_g \approx -15$ and therefore miss a large fraction of the faintest nuclei. Interestingly, a comparison with the GC mass function (GCMF; Jordan et al. 2007; dashed Gaussian curve) shows that the average NSC is nearly four times as massive as the typical GC in Virgo galaxies. The two mass functions naturally have very different widths, and it is perhaps not surprising that the faintest NSCs have masses virtually identical to those of the faintest GCs—which raises the question, how different are these NSCs from ordinary faint GCs?

5. Discussion

The present study contains three important results pertaining to the formation of NSCs and its relation to their host galaxies. First, to a high degree it is galaxy mass that regulates NSC formation and growth, in the sense that both very massive and very faint galaxies have low likelihoods of hosting nuclei. However, a secondary dependence on environment seems to indicate that the efficiency of NSC formation is also affected to some degree by the mass of the host halo, such that at fixed stellar mass galaxies in denser environments have a higher probability of being nucleated. Finally, even if environment somewhat regulates the likelihood of a given galaxy hosting an NSC, the universality of the NSC-to-galaxy mass relation indicates that the mass of the central star cluster is primarily controlled by the galaxy mass—albeit with a large scatter, which probably is an indication of the stochastic nature of NSC growth. We now turn to discuss the implications of these results in the context of NSC formation scenarios.

5.1. The Connection between NSCs, GCs, and DM Halo Mass

As has been previously discussed, it is natural to wonder about the relationship between the different families of star clusters in galaxies and about the role of total galaxy mass in the establishment of these relations. This is particularly true for GCs and NSCs, because the early decay and merging of dense star clusters seems a viable—perhaps even unavoidable—mechanism in the centers of galaxies. Also, the total mass of a GCS has been shown to correlate with the DM halo mass of the galaxy (Peng et al. 2008; Spitler & Forbes 2009; Georgiev et al. 2010; Hudson et al. 2014), and one may naïvely expect similar behavior for other compact stellar systems.

5.1.1. NSCs and GCs

In Figure 6 we reproduce the NSC occupation distribution in Virgo but now also include the fraction of galaxies that host GCs (triangles). GC candidates are selected from the mixture model classification by E. W. Peng et al. (2018, in preparation), and their numbers are counted to $g < 24.5$ (~0.6 mag fainter than the GC luminosity function [GCLF] turnover magnitude in Virgo) within a distance $<2.5\,R_e$ from the center of the galaxy (excluding the NSC). A local background level is determined in an annulus between 4 and 10 R_e and subtracted to account for contamination by stellar and extragalactic interlopers and by the rich GCS of M87. The final number $N_{\rm GC}$ of GCs is corrected to the full GCLF. Consistent with previous work, Figure 6 shows that all galaxies more massive than $M_\star \approx 10^9\,M_\odot$ host at least one GC (Peng et al. 2008; Georgiev et al. 2010). Remarkably, the fraction of galaxies containing GCs decreases toward lower masses at exactly the same rate as the nucleation fraction. Within the uncertainties, the two curves are indistinguishable from each other, which lends support to the idea that these two types of stellar systems are closely interconnected—perhaps both being the result of similar underlying physical processes.

While the GC and NSC occupation distributions are identical from a statistical point of view, this is not entirely the case on a galaxy-per-galaxy basis. In the same figure we show with squares the fraction of galaxies that simultaneously host an NSC and GCs. As before, here we do this exercise for galaxies with stellar masses ranging from $M_* = 10^5\,M_\odot$ to $M_* = 10^9\,M_\odot$, and all figures discussed in this section are only valid for objects within this mass range. The NSC+GC occupation distribution is slightly different from the NSC one, in the sense that at fixed galaxy stellar mass there is a lower fraction of galaxies that host the two types of star clusters. The breakdown of the star cluster occupation fraction in the core of Virgo is as follows: 43% of the galaxies in the mass range under study do not host any type of compact star cluster; 18% are non-nucleated galaxies that have GCs; 22% have both an NSC and GCs (the squares in Figure 6); and 17% of the galaxies have NSCs but no GCs. Of course, with the current data set we cannot rule out the possibility that the latter subpopulation at some point did have GCs that have been stripped during the orbital evolution within the cluster, or that their GCs merged to form the NSC. A perhaps even more intriguing possibility is that the NSC is indistinguishable from a regular old GC located at the bottom of the potential well. Detailed studies of the stellar populations in these low-mass NSCs are required to explore this hypothesis.

In Figure 7(a) we also study the relation between the mass of the NSC and the total mass of the GCS ($M_{\rm GCS}$), which we derive using the following Monte Carlo method. For each nucleated galaxy we randomly sample a normal distribution with a mean value $N_{\rm GC}$ and standard deviation $\Delta N_{\rm GC}$, which are extracted from the GC candidate catalog. The resulting number of GCs is rounded to the closest integer number $Z_{\rm GC}$, and if the galaxy has at least one GC ($Z_{\rm GC} \geqslant 1$), we assign each a mass according to a normally distributed GCMF. Jordan et al. (2007) show that the GCMF is not universal but rather exhibits a dependence on the luminosity/stellar mass of the host galaxy such that fainter systems feature lower turnover masses and narrower mass functions. Therefore, for each nucleated galaxy in the NGVS we draw GCs from a normal GCMF with turnover masses and logarithmic dispersions consistent with the (extrapolated) relation shown in Figure 14 from Jordan et al. (2007). The masses of the $Z_{\rm GC}$ clusters are summed to obtain a total mass for the GCS, and this Monte Carlo process is repeated 10,000 times for each galaxy. We record the mean GCS mass and its standard deviation, which are plotted against the masses of the NSCs in the top panel of Figure 7. We note that at low $M_{\rm GCS}$ values there is an unavoidable level of discreteness in the mean masses caused by galaxies that are consistent with having a single GC. In these cases the mean mass simply corresponds to the turnover mass of the GCMF evaluated at the corresponding galaxy stellar mass. The properties of the GCSs in the core of Virgo from NGVS data will be discussed in more detail in future papers of this series.

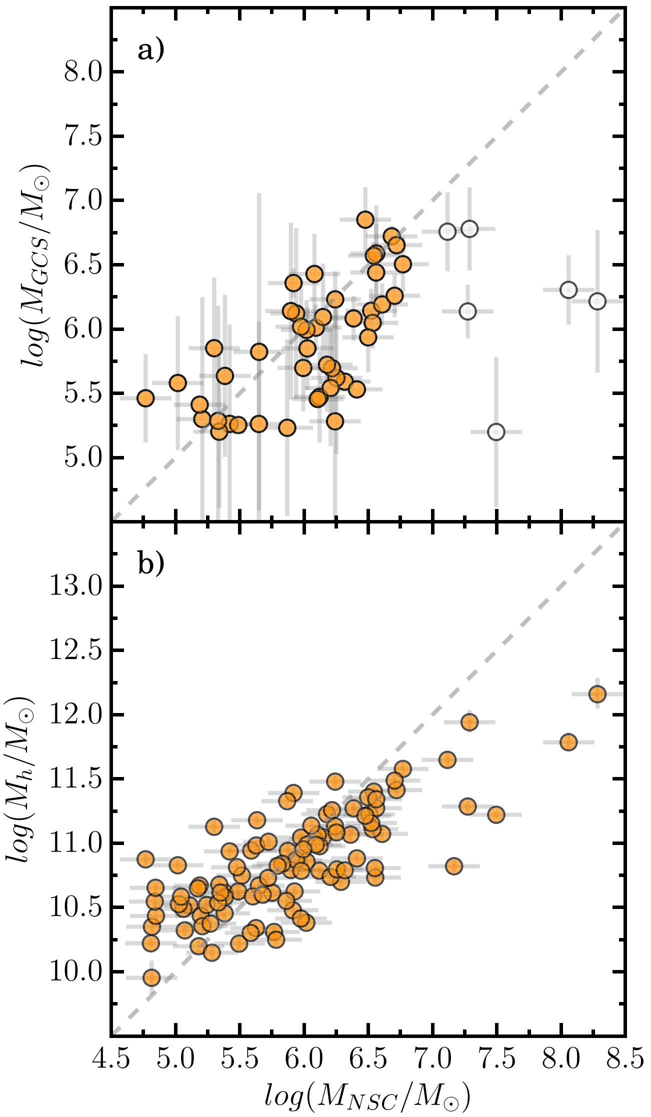

Figure 7. Masses of NSCs in the core of the Virgo cluster. Top: The estimated total mass of the GCS within 2.5 R_e is shown against the mass of the nucleus. The two quantities are consistent with each other for masses $M_{\rm NSC} < 10^7\,M_\odot$. The number of GC candidates is artificially biased low in more massive galaxies because of the aperture used to estimate their numbers (open symbols; see text for details). Bottom: The ordinates show the peak DM halo mass for each galaxy from abundance matching plotted vs. the mass of the nucleus. The two masses are correlated, but the relation differs from the constant mass fraction (shown as a dashed line for $M_{\rm h}/M_{\rm NSC} = 10^5$).

Figure 7(a) shows that $M_{\rm NSC}$ and $M_{\rm GCS}$ track each other remarkably well for masses $M_{\rm NSC} < 10^7\,M_\odot$, which corresponds to $M_* < 3 \times 10^9\,M_\odot$. In comparison more massive galaxies seem to feature depleted GCSs, but this is an artifact caused by the way the number of GCs is estimated. As described above, GC candidates are only selected within a projected distance $R < 2.5\,R_e$ from the center of the galaxy. While this is distant enough to account for the majority of GCs in low-mass systems, more massive galaxies certainly have GCSs extending far beyond this limit. As a result, we are progressively missing a larger fraction of the GCS as we move toward larger masses, and hence the apparent bend in the trend displayed in Figure 7(a).

In summary, for low-mass galaxies the data once again show a close connection between the two types of compact stellar systems, now in terms of their total masses. We conclude that while the presence of GCs is not a sufficient condition to form an NSC in low-mass galaxies (Miller et al. 1998; den Brok et al. 2014), the two families of star clusters are probably simply different manifestations of the prevalent mode of star formation at early times. Indeed, both the star cluster occupation fractions and the relation between the total masses of GCSs and NSCs can be qualitatively understood under a scenario where only the galaxies that happen to form enough proto-GCs within the dynamical friction cone develop an NSC—which, in turn, grows proportionally to the size of the GC population. We will further develop this idea in Section 5.3.

5.1.2. NSCs and DM Halo Mass

We now attempt a comparison between $M_{\rm NSC}$ and the DM halo masses $M_{\rm h}$. To determine $M_{\rm h}$ we make use of the SHMR obtained by Grossauer et al. (2015) for the NGVS via abundance matching. This technique relies on the assumption that there exists a univocal relation between stellar and DM halo masses, such that the *n*th-ranked galaxy occupies the *n*th most massive halo. We warn that this approximation most likely breaks down at the lowest masses probed by the NGVS due to the inefficiency of galaxy formation at these scales. For reference, Fattahi et al. (2016) show that in the APOSTLE simulation half of the halos with masses $M_{\rm h} = 10^{9.5}\,M_\odot$ remain fully dark. This in turn results in a systematic offset between the actual halo masses of the simulated galaxies and the $M_{\rm h}$ that would be inferred from the different abundance matching models. We finally note that because the Virgo sample is essentially comprised of satellites, the matching procedure is carried out at peak halo mass, and accordingly $M_{\rm h}$ represents the maximum DM halo mass ever attained by the galaxy—which occurs at the redshift of infall and not at $z = 0$. Present-day $M_{\rm h}/M_*$ ratios are expected to be much smaller due to the preferential stripping of DM halos relative to the stellar component as galaxies orbit within the cluster potential well (e.g., Smith et al. 2013, 2015).

With all these caveats in mind, in the lower panel of Figure 7 we show the NSC masses in the core of Virgo plotted against the estimated $M_{\rm h}$. Uncertainties in the stellar mass determinations and in the SHMR are plotted as error bars in Figure 7. This panel shows that there is a linear relation between $\log M_{\rm NSC}$ and $\log M_{\rm h}$, but it deviates from the constant mass fraction relation. For reference, the diagonal dashed line shows the expected relation if nuclear and halo masses were offset by a constant mass ratio $M_{\rm h}/M_{\rm NSC} = 10^5$. This difference actually is a direct result of the different low-mass slopes for the SHMR and the NSC-to-galaxy stellar mass relation. The abundance matching exercise by Grossauer et al. (2015) indicates that $M_{\rm h} \propto M_*^{0.39}$, whereas we obtain $M_{\rm NSC} \propto M_*^{0.46}$. Hence, we find a stronger dependence of the mass of the nucleus on halo mass, $M_{\rm NSC} \propto M_{\rm h}^{1.2}$. We note that β, the SHMR slope at the low-mass end, is still poorly constrained and its value is highly debated in the literature. Nevertheless, most recent works find it to be in the range $0.3 \lesssim \beta \lesssim 0.45$ (e.g., Behroozi et al. 2013; Moster et al. 2013; Brook et al. 2014; Sawala et al. 2015), and therefore the claim that NSC masses depend strongly on DM halo mass seems robust—provided the abundance matching approximation remains valid.

5.2. Comparison with Models for NSC Formation

We now interpret these results in the light of current models for NSC formation and explore to what extent they reproduce the observations in Virgo. Specifically, we compare the NGVS data against the models from Mclaughlin et al. (2006, hereafter M06) and Antonini et al. (2015, hereafter A15). M06 present a fully analytic model for the self-regulated growth of NSCs, where feedback from stellar winds and supernovae drives a superwind from the nucleus with a momentum flux directly proportional to the Eddington luminosity. When the NSC reaches a critical mass, the superwind can escape the galaxy, thus halting accretion and freezing $M_{\rm NSC}$. A15, on the other hand, make predictions for both the nucleation fraction and the NSC-to-galaxy stellar mass relation within a cosmological framework for galaxy formation. Their model comes in two flavors. The first one simply consists of a purely dissipationless process, whereby star clusters migrate to the galactic center and merge under the effect of dynamical friction (hereafter the `CliN` model). It is therefore very similar in spirit to Gnedin et al.'s (2014), but like most of these models it suffers from the limitation of not capturing the hierarchical buildup of galaxies or any dissipative process related to star formation. The second model (`GxeV`) addresses the latter aspects, as it first follows the growth and merger histories of galaxies and their DM halos and then incorporates a recipe for the formation of NSCs with a treatment for dissipative processes leading to nuclear star formation. This proves to be an important element, because according to their calculations more than half of the total NSC mass is accounted for by in situ star formation, and dissipative processes appear to become increasingly important with galaxy mass. The A15 models also take into account the disruptive effects of MBHs, which will become relevant when addressing NSC occurrence in high-mass galaxies.

5.2.1. The NSC Occupation Distribution

In Figure 8 we again reproduce the nucleation fraction in Virgo, now in direct comparison with the two sets of models from A15 (M06 do not make predictions for this quantity). The dissipationless `CliN` scenario (dashed line) is able to reproduce, at least qualitatively, the peaked form of the NSC occupation distribution. However, it predicts too high of an efficiency for NSC formation at intermediate to high galaxy masses. At the same time it underpredicts the nucleation fraction for masses below $\log(M_*/M_\odot) \approx 8.5$. The solid line corresponds to the NSC occupation fraction in the dissipative model. Here in situ star formation contributes significantly to the growth of NSCs in massive galaxies, and therefore the nucleation fraction departs even more from the observed behavior. If taken at face value, the results at the low-mass end are even more discouraging for the `GxeV` model, which predicts $f_{\rm n} \approx 100\%$ for all masses $M_\star \lesssim 10^{10}\,M_\odot$. Yet the observations indicate a steady decline of $f_{\rm n}$ toward low masses. However, A15 warn against putting too much trust in these numbers, because the identification of NSCs against

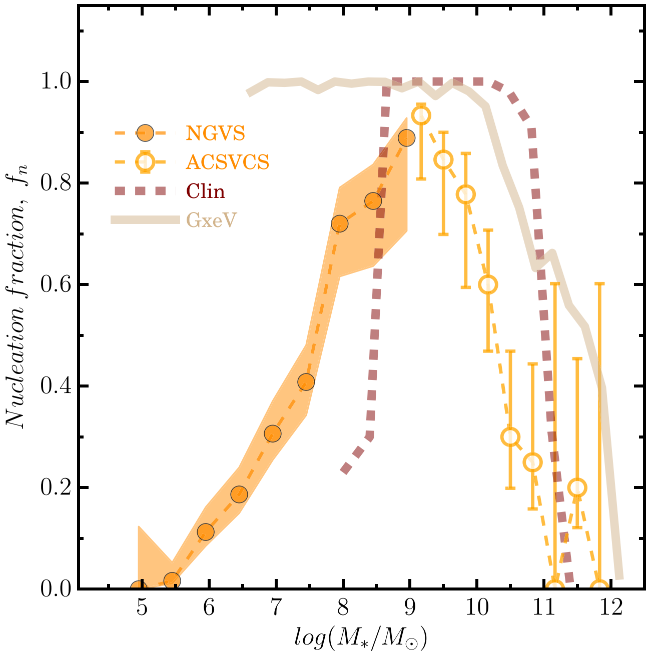

Figure 8. Same as Figure 6, but now the lines show the predictions for the NSC occupation fraction from the models by Antonini et al. (2015). The dashed line corresponds to a purely dissipationless model (`CliN`) of NSC growth via dynamical friction–driven mergers of pre-existing dense star clusters. The solid line is for a dissipative semianalytic model (`GxeV`) that incorporates gas inflows and in situ star formation. See text for discussion.

the galaxy background in the dissipative `GxeV` model is poor and the algorithm does not follow the evolution of individual star clusters, only the average nuclear mass infall rate.

The sudden drop in $f_{\rm n}$ at high masses $M_* \gtrsim 10^9\,M_\odot$ is a well-known result that is traditionally interpreted in the literature as the result of cluster disruption by the MBHs that inhabit the galactic centers. We note that the onset of this decline is perfectly consistent with recent results indicating that the MBH occupation fraction is high above $M_* \sim 10^9\,M_\odot$ (Miller et al. 2015; Nguyen et al. 2018). In the A15 models MBHs contribute to halting NSC formation and growth in two important ways. First, their strong tidal field enhances mass loss from star clusters as they decay toward the center, while simultaneous dynamical heating decreases their binding energy. This all contributes to a significant reduction in the amount of mass deposited in the NSC, if not implying the full disruption of the inspiraling star clusters. It is not clear at this stage why the Virgo galaxies seem to have a lower NSC occupation fraction at high masses compared to the models. One possibility is that the semianalytic formalism fails to capture the structural nonhomology of early-type galaxies. Emsellem & van de Ven (2008) show that for density profiles with Sérsic indices $n \gtrsim 3.5$ tidal forces become disruptive nearly everywhere and therefore hinder the efficient collapse of gas and its subsequent transformation into stars. Given the observed n–M_* relation in Virgo (Ferrarese et al. 2006b), this mechanism should operate in a majority of the early-type galaxies more massive than $M_* \approx 10^{10}\,M_\odot$. Alternatively, it is possible that the difference is an effect associated with the efficiency of star cluster disruption by MBHs as implemented in the semianalytic model.

For low-mass galaxies, however, this framework is unlikely to apply for two reasons. First, in several scenarios of MBH formation the occupation fraction is expected to be a relatively strong increasing function of galaxy mass (Volonteri 2010 and references therein). Many of these low-mass galaxies probably do not host an MBH at all. But even if they do, its mass would need to be larger than $M_\bullet \approx 10^8\,M_\odot$ to efficiently disrupt inspiraling star clusters and halt any further NSC growth (see the discussion in A15 about the importance of this characteristic mass scale). According to the observed $M_\bullet$–M_* relation (McConnell & Ma 2013), this value is well above the expected black hole masses in $M_* \lesssim 10^9\,M_\odot$ galaxies.

Galaxies in the core of Virgo with stellar masses below this limit have light profiles well described by Sérsic indices in the range $0.5 < n \lesssim 1.5$ (Ferrarese et al. 2016), which, as Emsellem & van de Ven (2008) show, feature compressive tidal forces in the central regions that are conducive to NSC formation. And yet the observations indicate that fewer lower-mass galaxies eventually form nuclei. Possible solutions to this puzzle range from stellar feedback preventing cold gas from reaching the nuclear regions of these galaxies (El-Badry et al. 2016) to the presence of very cuspy halos such that DM is a dominant mass component in the very central regions of these galaxies.

We propose instead that a more likely explanation for the paucity of NSCs toward low galaxy masses is simply a low initial number of dense star clusters. We have shown that the existence of GCs is tightly linked to the presence of NSCs, and numerous studies have now established that the total mass of a GCS correlates tightly with the DM mass of the galaxy (Peng et al. 2008; Spitler & Forbes 2009; Georgiev et al. 2010; Hudson et al. 2014). If this holds for very low mass galaxies and they form a low number (but high mass fraction) of bound star clusters, then it is natural to expect that many faint galaxies simply lack the ingredients to form an NSC seed in the first place.

5.2.2. The NSC-to-galaxy Stellar Mass Ratio

In Figure 9 we show the NSC-to-galaxy mass ratio as a function of galaxy stellar mass for the NGVS and the literature samples, with symbols as indicated in the legend of Figure 4. These two figures are essentially equivalent, but Figure 9 does a better job at highlighting the increasing prominence of NSCs toward lower masses. As in Figure 4, the horizontal dashed lines indicate constant NSC mass fractions of 0.1%, 1%, and 10%, from bottom to top. To better illustrate the dramatic dependence of the nuclear mass fraction on host stellar mass, large diamonds show the mean $M_{\rm NSC}/M_*$ ratio in bins of constant galaxy stellar mass. The mass ratio spans nearly three orders of magnitude, with a mean value that drops to ≈0.36% for galaxies with $M_* \approx 3 \times 10^9\,M_\odot$ and then increases for both more and less massive galaxies. This minimum value for $M_{\rm NSC}/M_*$ is very similar to the constant mass ratio found in the Virgo and Fornax ACS surveys (Cote et al. 2006; Turner et al. 2012). But Figure 9 indicates that the ratio is anything but constant. The increasing prominence of NSCs is exacerbated at the lowest mass scales, where a few nuclei are ≈50% as massive as their hosts. The trend is present in all the samples of cluster low-mass galaxies included in Figure 4, but it is only thanks to the significant extension toward the low-mass end enabled by the NGVS that we can assess its statistical significance with confidence. We will now discuss these results

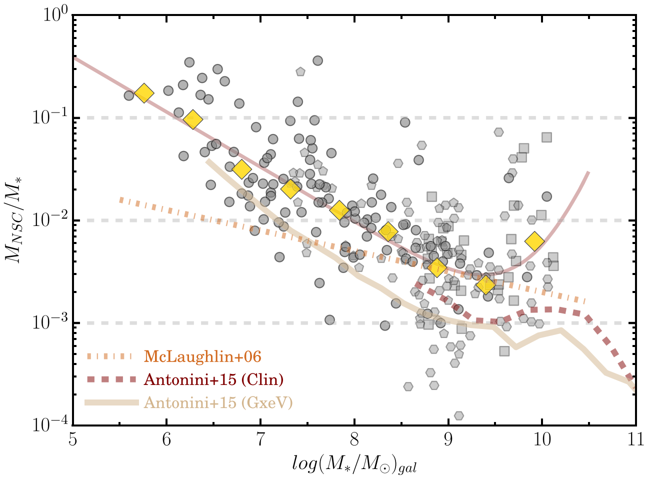

Figure 9. NSC-to-galaxy stellar mass ratio for the NGVS and literature samples. Symbols are as in Figure 4. The large diamonds show the mean relation in bins of stellar mass, and they highlight the strong dependence of the nuclear mass fraction on host mass. The thin solid line corresponds to the best-fit $M_{\rm NSC}$–M_* relation. The mass ratio spans nearly three orders of magnitude, with the most prominent nuclei being almost 50% as massive as their host galaxies. The thick lines correspond to different predictions from a dissipative model (solid) and two different dissipationless models for NSC formation (dashed and dashed–dotted lines). See text for details.

in the context of dissipative and dissipationless models of NSC formation. More specifically, there is a clear prediction from models of NSC growth via GC inspiraling that the nuclear mass fraction should scale as $M_{\rm NSC}/M_* \propto M_*^{-0.5}$ (Antonini 2013; Gnedin et al. 2014). A simple inspection of Figure 9 indicates that this behavior does not hold at high galaxy masses, and this is a clear indication that additional (dissipative) mechanisms have to be invoked to explain these NSC masses.

The thick dashed–dotted line in Figure 9 shows the prediction for the $M_{\rm NSC}/M_*$ ratio from the feedback-regulated model by M06. We use their Equation (10) with the following parameters: $\lambda = 0.05$ for the wind thrust efficiency, $Z = 0.5\,Z_\odot$ for the stellar metallicities, and $v_{\rm w} = 200\,{\rm km\,s^{-1}}$ for the velocity of the superwind. These values are chosen to reproduce the NSC mass fraction at the intermediate-mass regime, where the kink of the $M_{\rm NSC}/M_*$ ratio occurs, but it is clear that at lower masses the analytical relation is too shallow compared to the data. This is because in this model the self-regulated mass of the nucleus scales as $M_{\rm NSC} \propto M_*^{-1/5}$, which is inconsistent with our best-fit slope (see Table 1). It follows that if feedback played a relevant role in setting the initial masses of NSCs, additional growth mechanisms are required to explain their present-day stellar content.

The solid and dashed thick lines in Figure 9 correspond to the predictions for the $M_{\rm NSC}/M_*$ ratio from the dissipative (`GxeV`) and dissipationless (`CliN`) models by A15, respectively. It is interesting—or perhaps worrying—that these two models seem to reproduce the observed trend at low masses. While predicting the correct slope for the $M_{\rm NSC}$–M_* relation can be seen as a significant success, it also means that this relation provides little to no discriminating power on possible formation scenarios. The similarity between the dissipationless and dissipative models indicates that, essentially, at low galaxy masses NSC growth is controlled by the average nuclear mass infall rate, independently of whether the NSC is constituted by stellar or gaseous material. The stellar population properties of the NSCs *do* differ in the dissipative and dissipationless scenarios, and detailed studies of the least massive NSCs will clarify if the complex star formation histories found in the nuclei of intermediate-mass galaxies (Monaco et al. 2009; Seth et al. 2010; Paudel et al. 2011) are mirrored at the smallest scales.

As already mentioned, the very low mass ratio predicted by all these models for $M_* \gtrsim 10^{10}\,M_\odot$ galaxies is troubling. However, these massive NSCs in Virgo and Fornax are quite peculiar systems that do not resemble the nuclei found in lower-mass objects in a number of ways. They feature more flattened morphologies and very large half-light radii, and their colors show increased scatter compared to lower-mass systems—with a predominance of nuclei that are even redder than their host galaxies (Cote et al. 2006; Turner et al. 2012). In light of these properties it has been proposed that these massive NSCs resemble the "dense stellar cores" that form in some numerical simulations as a result of dissipative processes involving mergers and/or nuclear gaseous inflows (Mihos & Hernquist 1994). The observed discrepancy between data and models implies that the formation mechanisms of such a mass excess in the central regions of the most massive galaxies are not fully captured by current NSC formation models, even when they incorporate dissipative processes.

Overall, the shape of the NSC-to-galaxy stellar mass ratio indicates the existence of two well-defined mass regimes. Below $M_* \approx 5 \times 10^9\,M_\odot$ NSCs become increasingly prominent, and we will now discuss this finding in the context of dynamical friction–driven coalescence of dense star clusters.

5.3. A Scenario for Biased NSC Formation

We have shown that the present-day galaxy mass (stellar or total) seems to be the main parameter controlling not only whether a galaxy harbors an NSC but also its subsequent growth. This is in line with previous work, but our results further demonstrate that this simple picture is incomplete. Our finding that at fixed stellar mass the nucleation fraction shows a secondary dependence on the mass of the host halo indicates that NSC occurrence is a more complex phenomenon that depends on properties related to the global environment. We are not aware of any model for NSC formation that reproduces this effect in early-type galaxies, but the result is very reminiscent of the discovery by Peng et al. (2008) that the GC specific frequencies in Virgo galaxies are also biased toward dense environments. Specifically, the average GC mass fraction for $M_* \lesssim 5 \times 10^9\,M_\odot$ galaxies increases from the galaxy cluster outskirts to the center. Peng et al. (2008) were able to show that, at least qualitatively, the trend can be explained by the preferential formation of GCs in the earliest collapsing halos that can efficiently form stars before reionization. In this biased scenario, the galaxies that inhabit the central cluster regions would have collapsed first, starting to form stars earlier and doing so at higher star formation rates (SFRs) and higher star formation surface densities ($\Sigma_{\rm SFR}$) than the systems that are presently found in the cluster outskirts. Old GCs are believed to form precisely in regions featuring high $\Sigma_{\rm SFR}$ and enormous pressure (Harris & Pudritz 1994; Elmegreen & Efremov 1997; McLaughlin 1999; Ashman & Zepf 2001; Kruijssen 2015; Pfeffer et al. 2018). This, together with the fact that satellites residing in higher-density environments are accreted at earlier times and form stars rapidly (Liu et al. 2016), naturally results in higher present-day GC mass fractions for the innermost systems.

Here we speculate that the same biased formation channel for star clusters is responsible for the observed environmental dependence of the nucleation fraction toward low galaxy masses. It is well established that the clustering of DM halos is a strong function of mass and formation time, especially for ancient, low-mass halos (Gao et al. 2005; Wechsler et al. 2006; Dalal et al. 2008; Lacerna & Padilla 2011). This is equivalent to saying that at fixed peak mass subhalos form earlier in more massive host halos, an effect known as assembly bias. All the low-mass cluster galaxies shown in Figure 2 inhabit regions with similarly high mean overdensity ($R/R_{\mathrm{vir}} \lesssim 0.25$) and are therefore expected to be the most ancient population in these clusters. For reference, subhalos in virial equilibrium in the cores of massive clusters have typical infall times of $t_{\mathrm{inf}} \gtrsim 6$ Gyr (Oman et al. 2013). Thus, at fixed galaxy stellar mass all these subhalos did reach a similar peak halo mass,[25] but those in the core of Coma attained it at earlier times than those in the core of Virgo (or Fornax). In fact, prior to infall the subhalos in denser environments were *at all times* more massive than those in slightly less dense regions.

If we extrapolate back in time to the epoch of GC formation ($z \gtrsim 2$), we will find a scenario equivalent to that proposed by Peng et al. (2008), namely that low-mass galaxies in Coma started forming stars earlier than those in Virgo, and at higher SFRs and Σ_{SFR}. These conditions were conducive to the formation of bound young massive clusters (YMCs), and if cluster formation efficiency was close to universal (McLaughlin 1999) and galaxies formed YMCs proportionally to their mass at that epoch (Kruijssen 2015), then one naturally expects a larger mass fraction in star clusters in the more biased (proto-)Coma galaxies.[26]

The YMCs that were born closer to the center of the potential well and survived the early disruption phase (Kruijssen et al. 2011) were able to merge within a few dynamical times. Simple dynamical friction arguments (e.g., Lotz et al. 2001) indicate that, for $M_* \lesssim 10^8\,M_\odot$ galaxies, a star cluster with the GCMF turnover mass would decay from a distance of ~1 kpc in less than a few billion years. In this context it is important to recall that DM halos grow their central potential very rapidly at early times, but during the subsequent long-lasting slow-accretion regime the material builds up predominantly in the outskirts and the central densities change very little (Wechsler et al. 2002; van den Bosch et al. 2014). Under these conditions, and considering the very low masses of the faintest nucleated galaxies in Virgo—almost comparable to those of regular GCs—the dynamical friction–driven orbital decay of bound star clusters has probably been a very efficient mechanism throughout a large fraction of the galaxy's history.

Baryons of course complicate this simple picture, and dissipative processes have probably contributed to some extent to the growth of NSCs in low-mass galaxies. The mass distribution of (non-cuspy) low-mass galaxies favors nuclear gas inflows (Emsellem & van de Ven 2008), and with all likelihood the last star formation events in these quiescent galaxies took place in the central regions.

Admittedly, this scenario is highly speculative. But the proposal that nucleated early-type cluster galaxies are a biased subpopulation is actually not new, but rather consistent with previous results in the literature. These galaxies have a tendency to inhabit the inner and higher-density cluster regions (Binggeli & Cameron 1991; Lisker et al. 2007), their velocity distribution reveals a preference for circularized orbits (Lisker et al. 2009), and there is tentative evidence that they feature higher GC mass fractions than non-nucleated cluster galaxies (Miller et al. 1998; Sánchez-Janssen & Aguerri 2012). The results presented here just add another element in support of this picture, but many questions remain unanswered. For example, why does this scenario result in ~50% of all the mass in old star clusters ending up in the NSC regardless of galaxy mass? What is the nature of the observed change in the mass fraction slope at high masses? If a larger fraction of stars in cluster galaxies indeed form in bound star clusters, the naïve expectation is that the NSC mass fraction should depend on environment, but this is not observed. Finally, this scenario must also provide an explanation for the mildly bluer colors and younger ages of NSCs relative to their host galaxies (e.g., Spengler et al. 2017).

5.4. UCDs, Satellite Disruption, and Mass Deposition on Stellar Halos

Soon after their discovery UCDs were already suspected to be the surviving nuclei of disrupted satellites (Bekki et al. 2003; Drinkwater et al. 2003; Goerdt et al. 2008). Subsequent work has shown that they probably constitute a mixed bag of objects with galactic and star cluster origins and that there is a trend for NSCs (GCs) to be dominant at the high-mass (low-mass) end (Haşegan et al. 2005; Evstigneeva et al. 2007; Mieske et al. 2008, 2012; Norris et al. 2014; Zhang et al. 2015; Pfeffer et al. 2016). An important link between UCDs and nucleated galaxies was recently discovered by Liu et al. (2015a) using NGVS imaging. They presented evidence that a fraction of the UCDs surrounding M87 and M49 are embedded in low surface brightness envelopes whose prominence correlates with the distance to these massive galaxies. Thus, the innermost UCDs show no evidence of such stellar halos, whereas the envelopes surrounding the most distant systems are so prominent that they unambiguously are nucleated galaxies. The nature of the intermediate objects in this morphological sequence is unclear at the moment, but the progression toward less prominent envelopes with galactocentric distance is consistent with the tidal stripping picture (e.g., Pfeffer & Baumgardt 2013). Alternatively, the objects with envelopes may simply be nucleated galaxies with very prominent NSCs, like those we find at the low-mass end. However, we note that (i) there is no overlap between the sample of UCDs from Liu et al. (2015a) and our nucleated low-mass objects, and (ii) unlike with the UCDs, we do not find a correlation between the distance to M87 and the prominence of the NSC.

We note in passing that the recent hydrodynamic cosmological simulations by Ricotti et al. (2016) offer an intriguing alternative for the origin of these envelopes. These authors

---

[25] This statement is of course only valid for galaxies that have not suffered significant stellar mass loss after infall. While this is generally true for the average satellite population (Watson & Conroy 2013), it may be less valid for low-mass galaxies in the cores of massive clusters (Smith et al. 2015).

[26] Note that if this scenario is correct, it also implies that the low-mass galaxies in clusters like Coma must feature higher GC mass fractions (or specific frequencies) than those in Virgo.

Table 2
Inferred Stellar Masses for the Progenitors of Stripped NSC Candidates in the Local Group

Cluster	$M_{\rm GC}/M_\odot$	$M_{\star,\rm p}/M_\odot$	References
ωCen	2.5×10^6	6.3×10^8	(1)
M54	2.0×10^6	4.0×10^8	(1)
NGC 2419	1.3×10^6	1.9×10^8	(1)
M19	0.9×10^6	0.9×10^8	(1)
Mayall II/G1	4.6×10^6	15.0×10^8	(2)
G78	2.4×10^6	5.9×10^8	(3)
G213	1.8×10^6	3.6×10^8	(3)
G280	2.2×10^6	5.0×10^8	(3)

Note. (1) Mackey & van den Bergh (2005), (2) Meylan et al. (2001), (3) Fuentes-Carrera et al. (2008).

followed the formation of very low mass galaxies ($M_* \lesssim 10^6\,M_\odot$) before reionization, and in their simulations the majority of the stars formed in dense star clusters. The more massive clusters remained bound after gas was expelled by ongoing star formation, but those with masses $\lesssim 10^4\,M_\odot$ dissolved and expanded until they became bound by the DM halo. If the surviving more massive clusters merged driven by dynamical friction, the object left behind closely resembled a (low-mass) UCD with an envelope (see also Milosavljevič & Bromm 2014).

Coming back to the threshing scenario, Ferrarese et al. (2016) show that the observed $M_{\rm NSC}$–M_* relation can be inverted and used in combination with the abundance of UCDs to provide an estimate of the amount of intracluster light in the core of Virgo contributed by disrupted satellites. An even simpler and direct application of this relation is to compute the mass in stars contributed to the stellar halos of other massive galaxies by the putative progenitors of UCDs. The three most massive UCDs in the Virgo cluster are not located close to M87 but reside in the infalling group dominated by the massive early types M60 and M59 (Chilingarian & Mamon 2008; Liu et al. 2015b; Sandoval et al. 2015). The stellar masses of these UCDs are in the $(0.5\text{–}1.5) \times 10^8\,M_\odot$ range, and if they are the remnants of threshed progenitors that followed the observed mean relation in Figure 4, then their parent galaxies had stellar masses in excess of $M_* \sim 10^{10}\,M_\odot$. M59 hosts the first and third most massive of the UCDs, and under this scenario approximately 15%–25% of its stellar mass would have been accreted in two distinct merger events. This figure is consistent with recent cosmological hydrodynamic simulations of stellar halo formation, which indicate a larger contribution of accreted mass in the stellar halos of more massive galaxies (Rodriguez-Gomez et al. 2016).

Given the observed universality of the $M_{\rm NSC}$–M_* relation, a similar exercise can be attempted in the Local Group, where some of the most massive GCs have long been suspected of being a distinct subpopulation. Specifically, ωCen, M54,[27] and NGC 2419 in the MW and Mayall II/G1 in M31 are canonical examples of stripped NSC candidates. Evidence for the nuclear origin picture for these systems includes very high surface mass densities, large internal metallicity spreads and significant elemental abundance variations, unusually high eccentricities, and the presence of kinematic subpopulations (Ibata et al. 1994, 1995; Norris & Da Costa 1995; Sarajedini & Layden 1995; Norris et al. 1997; Lee et al. 1999; Pancino et al. 2000; Meylan et al. 2001; van den Bergh & Mackey 2004). Recently, the lower-mass GC M19 has been shown to have an intrinsic abundance spread of $\sigma[{\rm Fe/H}] = 0.17$ dex, only surpassed by ωCen and M54 in the Galactic GCS (Yong et al. 2016). This is highly suggestive of a nuclear origin as well, and so we include M19 in the list of putative surviving NSCs. Finally, Fuentes-Carrera et al. (2008) found that three additional high-velocity dispersion clusters in M31 exhibit very large abundance spreads, and they are included in our analysis as well (Table 2).

We invert our best-fit $M_{\rm NSC}$–M_* relation to infer the stellar masses for the progenitor galaxies of these star clusters under the assumption that they are indeed fully stripped NSCs. To do this we first compute the masses of the clusters using M_V measurements from the literature, as indicated in the last column of Table 2. For all clusters we then assume a common $(g - V) = 0.4$ color and $M_*/L_g = 2.7$ (e.g., van de Ven et al. 2006; Noyola et al. 2010). The second column shows the present-day GC masses, here assumed to be identical to $M_{\rm NSC}$. The third column corresponds to the expected mean stellar masses for the parent galaxies, $M_{\star,\rm p}$, which range from $10^8\,M_\odot$ to $10^9\,M_\odot$. We recall that the significant intrinsic scatter of the $M_{\rm NSC}$–M_* relation implies that these values can be a factor $\approx$2.5 larger or smaller. In any case, it is clear that only a handful of these (presumably) disrupted systems can contribute $\gtrsim 10^9\,M_\odot$ to the stellar halos of the central galaxies in the Local Group.

This aligns well with mounting evidence from both numerical (Bullock & Johnston 2005; Cooper et al. 2010; Deason et al. 2016; van Oirschot et al. 2017) and observational work (Fiorentino et al. 2014; Deason et al. 2015) that the bulk of the accreted stellar halo in MW-sized galaxies is contributed by a small number of relatively massive satellites with stellar masses of 10^8–$10^{10}\,M_\odot$. For reference, the MW is thought to have a stellar halo $M_{*,\rm h} \approx 1 \times 10^9\,M_\odot$, corresponding to roughly 2% of its stellar mass (Carollo et al. 2010; Licquia & Newman 2015). M31's halo is slightly more massive, $M_{*,\rm h} \approx 4 \times 10^9\,M_\odot$, amounting to nearly 4% of its stellar mass (Courteau et al. 2011; Sick et al. 2014). Comparison with Table 2 indicates that 30%–100% of the mass in these halos can be accounted for by the progenitors of (known) NSC candidates. This is only a crude comparison and the uncertainties are important—e.g., we assume that the galaxy stars are fully stripped, but depending on the orbital configuration a fraction of that material can remain bound and form an "envelope" around the nucleus (e.g., Pfeffer & Baumgardt 2013; Liu et al. 2015a); also, a non-negligible fraction of the material released by a threshed satellite is deposited in the inner rather than the outer halo, where stars mix with a pre-existing in situ population (Zolotov et al. 2009). But if indeed the subset of massive, peculiar GCs in the Local Group are the remnants of disrupted galaxies, we propose that relatively massive *nucleated* satellites constituted a significant fraction of the building blocks for the stellar halos in the MW

---

[27] The case of M54 is notably special. The cluster is still embedded within the disrupting stellar body of the Sagittarius dSph, and therefore its accreted origin is unambiguous. However, Bellazzini et al. (2008) show that M54 coexists with a distinct nuclear component that can be differentiated in the velocity–metallicity phase space. These authors suggest that they formed independently and M54 plunged to the central region driven by dynamical friction. Because it is impossible for us to quantify how common this feature is among the Virgo nucleated galaxies, here we simply take the view that the two components constitute the NSC of Sagittarius.

and in M31. A better understanding of the relation between the stellar populations of NSCs and their host galaxies can guide us to identify coherent structures in the multidimensional spatial–kinematical–chemical phase space originating from material stripped from these galaxies.

6. Conclusions

In this study we use deep, high spatial resolution optical imaging from the NGVS to detect and characterize the NSCs in a volume- and mass-limited sample of nearly 400 galaxies in the core of the Virgo cluster spanning seven decades in stellar mass. Here we focus on the occurrence of NSCs as a function of galaxy mass and environment and on mass scaling relations with their host galaxies. Our main conclusions are as follows:

1. The NSC occupation distribution is a strong function of galaxy stellar mass. It peaks at $f_{\rm n} \approx 90\%$ for $M_* \approx 10^9\,M_\odot$ galaxies and then declines monotonically for both more and less massive galaxies. The distribution is shaped by the interplay between the disruptive effects of MBHs at the high-mass end and (possibly) a low initial number of dense star clusters at the low-mass end, where $f_{\rm n} \propto \log M_*^{1/4}$. We identify a characteristic mass $M_* \approx 5 \times 10^5\,M_\odot$ below which no galaxy in the core of Virgo is nucleated.
2. We compare the NSC occupation distribution in Virgo with other environments spanning a wide range of host halo masses, including the Coma and Fornax clusters and the MW, M31, and M81 groups. We unveil a secondary dependence of $f_{\rm n}$ on environment, such that at fixed galaxy stellar mass nucleation is more frequent in more massive host halos.
3. NSCs have integrated colors that primarily depend on their stellar mass, such that more massive nuclei are redder. Because $M_{\rm NSC}$ and M_* are also correlated, redder NSCs inhabit redder galaxies, but the poor correlation between these quantities indicates this is only a weaker relation.
4. There is a universal, nonlinear relation between $M_{\rm NSC}$ and M_*, such that the nucleus-to-galaxy stellar mass ratio drops to $M_{\rm NSC}/M_* \approx 3.6 \times 10^{-3}$ for galaxies of mass $M_* \approx 5 \times 10^9\,M_\odot$. NSCs in both more and less massive galaxies are much more prominent, with the latter scaling as $M_{\rm NSC} \propto M_*^{0.46}$. This implies that the faintest nucleated galaxies in the core of Virgo host NSCs that are nearly 50% as massive as the galactic body itself. However, we also measure an intrinsic scatter in the $M_{\rm NSC}$–M_* relation of 0.4 dex, which we interpret as evidence of the stochastic growth of NSCs.
5. This universal relation can be inverted to infer the masses for the progenitors of UCDs and massive GCs in the Local Group under the hypothesis that they are the NSCs of tidally disrupted satellites. From this exercise we conclude that relatively massive nucleated satellites constituted a significant fraction of the building blocks for the stellar halos of L^* galaxies.
6. We construct the first volume- and mass-limited NSC mass function in Virgo, which peaks at $M_{\rm NSC} \approx 7 \times 10^5\,M_\odot$ and has a standard deviation of 0.68 dex. Comparison with the GCMF indicates that the average NSC in Virgo is 3–4 times as massive as the typical GC.
7. We find a close connection between NSCs and GCs, in the sense that the fraction of galaxies hosting either type of star cluster system decreases toward lower masses at the same rate. Additionally, the total mass of the GCS is similar to the NSC mass for $M_* \lesssim 10^9\,M_\odot$ galaxies, but the relation breaks down at the high-mass end, due to a combination of excessively prominent NSCs and an apparent scarcity of GCs.
8. The mass of an NSC exhibits a (logarithmic) linear relation with the estimated peak DM halo mass, but its slope is steeper than the corresponding slope if the NSC mass fraction were constant, $M_{\rm NSC} \propto M_{\rm h}^{1.2}$.
9. Current models for NSC formation, including dissipative and dissipationless processes, reproduce, at least qualitatively, the observed trends. Unfortunately, neither the nucleation fraction nor the $M_{\rm NSC}$–M_* relation seems to have enough discriminative power to distinguish between these scenarios or quantify their relative contribution to NSC formation. We are however able to show that a model for self-regulated growth of nuclei driven by stellar feedback is not sufficient to explain the observed NSC masses. We speculate that galactic nuclear formation is best explained by a biased process whereby dense star clusters preferentially form and aggregate in the earliest collapsing halos, and that the subsequent level of growth is determined by the average nuclear mass infall rate.

We find that $M_* \sim 10^{9.5}\,M_\odot$ seems to be a very interesting mass scale where (i) the NSC occupation fraction peaks, (ii) the NSC mass fraction reaches a minimum, and (iii) the NSC and GC occupation fractions stop tracking each other. This remarkable coincidence is highly suggestive of the existence of an underlying physical mechanism(s) regulating the growth of both NSCs and their host galaxies. These three observational results shall inform numerical and theoretical models for the formation of NSCs. In future NGVS papers we will expand the study of NSCs to the entire virial volume of Virgo, where we can investigate whether the occupation fraction depends on clustercentric position or local environmental density. We will also extend the studies on NSC occurrence and its relation to NSC hosts to star-forming galaxies as well as improve the statistics at the high-mass end. Constructing a large sample of NSCs in galaxies in the 10^9–$10^{11}\,M_\odot$ range is the next critical step to fully understand the nature of the rare and extended NSCs that produce the bend in the $M_{\rm NSC}$–M_* relation. Finally, we plan to exploit the multiwavelength $u'griz'$ photometry provided by the NGVS to carry out studies of their stellar population content through modeling their SEDs (e.g., Spengler et al. 2017).

Table 3
Nucleation of Early-type Satellites in the Local Volume

Name	Host	$\log M_*/M_\odot$	Nucleation
NGC 205	M31	8.85	1
M32	M31	8.33	1
NGC 147	M31	8.33	0
NGC 185	M31	8.29	0
KDG 61	M81	7.57	1
Sag dSph	MW	7.49	1
F8D1	M81	7.45	0
KDG 64	M81	7.45	1
KDG 63	M81	7.25	0
KK 77	M81	7.21	0
Cas dSph	M31	7.09	0
IKN	M81	7.05	0
Fornax	MW	7.01	0
DDO 78	M81	7.01	0
BK6N	M81	6.85	0
Leo I	MW	6.81	0
Peg dSph	M31	6.69	0
And I	M31	6.69	0
KKH 57	M81	6.49	0
Cetus	M31	6.49	0
Sculptor	MW	6.33	0
CKT 2009-d0934+70	M81	6.25	0
And XXIII	M31	6.21	0
KKR 25	M31	6.17	0
And XXI	M31	6.13	0
And III	M31	6.13	0
And II	M31	6.09	0
Tucana	MW	6.09	0
And V	M31	6.09	0
And XVIII	M31	6.05	0
Leo II	MW	6.05	0
CKT 2009-d0955+70	M81	6.05	0
And XXV	M31	6.05	0
Carina	MW	6.01	0
Draco	MW	5.89	0
Sex dSph	MW	5.89	0
And XV	M31	5.89	0
CKT 2009-d1006+67	M81	5.85	0
And XIX	M31	5.73	0
CKT 2009-d1014+68	M81	5.73	0
And XVI	M31	5.69	0
And IX	M31	5.65	0
Bol 520	M31	5.65	0
And X	M31	5.57	0
CVn I	MW	5.57	0
And XIV	M31	5.49	0
And XXVIII	M31	5.49	0
And XXIX	M31	5.41	0
CKT 2009-d0944+69	M81	5.37	0
And XXVII	M31	5.33	0
UMin	MW	5.25	0
And XVII	M31	5.21	0
And XXIV	M31	5.21	0
And XIII	M31	5.13	0
And XXVI	M31	5.01	0

The authors thank Fabio Antonini for providing the data from his semianalytic models in electronic format. R.S.J. would like to thank Diederik Kruijssen, Nadine Neumayer, Joel Pfeffer, and Anil Seth for useful discussions and suggestions. The authors acknowledge the thorough and constructive review of the manuscript by an anonymous referee. T.H.P. acknowledges support from the FONDECYT Regular Project grant (No. 1161817) and CONICYT project Basal AFB-170002. S.M. acknowledges financial support from Institut Universitaire de France, of which she is a senior member. This work is supported in part by the Canadian Advanced Network for Astronomical Research, which has been made possible by funding from CANARIE under the Network-Enabled Platforms program. This research used the facilities of the Canadian Astronomy Data Centre, operated by the National Research Council of Canada with the support of the Canadian Space Agency. The authors further acknowledge use of the NASA/IPAC Extragalactic Database, which is operated by the Jet Propulsion Laboratory, California Institute of Technology, under contract with the National Aeronautics and Space Administration.

Appendix
NSCs in the MW, M31, and M81 Systems

In Figure 2 we include two data points corresponding to the nucleation fraction in the MW, M31, and M81 groups. As has been broadly discussed in the literature, robustly identifying NSCs is in many cases far from trivial. Here we detail the process we have followed in this work to perform nucleation classification for nearby satellites. The interested reader is referred to Section 4.2 in Turner et al. (2012) for a more detailed discussion on other systems that feature structural and kinematical peculiarities in their nuclear regions but that we do not classify as nucleated.

We select all candidates from Karachentsev et al.'s (2013) Updated Nearby Galaxy Catalog. We transform the listed B-band magnitudes to the V-band assuming $(B - V) = 0.7$ and compute stellar masses using $M_*/L_V = 1.6$ (Woo et al. 2008). We further select only galaxies with stellar masses in the $10^5 < M_*/M_\odot < 10^9$ range with early-type morphologies ($T < 0$) and whose main perturber is any of the three central spirals. The final sample consists of 55 nearby satellites (Table 3).

Of these, only one satellite galaxy is considered to be nucleated in the MW system, namely the Sagittarius dSph (Mateo 1998; Monaco et al. 2005). In M31 we count M32 and NGC 205 as unambiguously having NSCs. Finally, for satellites in the M81 group we have visually inspected the *HST* images for all the candidate galaxies from Chiboucas et al. (2013). Only two systems, KDG 61 and KDG 64, are identified as nucleated.

Table 4
Photometry of NGVS Galaxies

ID	M_u	Δu	M_g	Δg	M_r	Δr	M_i	Δi	M_z	Δz	log $(M_*/M_\odot)$	Nucleation
NGVS J12:26:20.07+12:30:37.1	−11.95	0.04	−12.97	0.02	−13.51	0.01	−13.76	0.02	−13.85	0.04	7.3	0
NGVS J12:26:20.39+12:34:27.3	−11.27	0.36	−12.02	0.15	−12.53	0.12	−12.55	0.20	−12.70	0.30	6.8	0
NGVS J12:26:22.61+12:47:11.0	−12.53	0.05	−13.49	0.02	−14.01	0.02	−14.26	0.03	−14.40	0.05	7.5	1
NGVS J12:26:23.64+13:22:24.7	−11.44	0.23	−12.49	0.03	−13.02	0.04	−13.17	0.04	−13.38	0.07	7.0	1
NGVS J12:26:24.04+12:25:00.5	−8.60	0.62	−9.61	0.20	−10.18	0.18	−10.37	0.34	−9.85	0.47	5.8	0
NGVS J12:26:26.21+12:39:10.6	−9.44	0.51	−10.60	0.13	−11.20	0.14	−11.40	0.22	−11.65	0.28	6.3	0
NGVS J12:26:26.30+11:44:08.0	−9.10	0.84	−9.81	0.44	−10.50	0.32	−10.74	0.55	−11.86	0.33	6.0	0
NGVS J12:26:26.97+12:54:23.6	−9.62	0.96	−10.52	0.12	−11.14	0.68	−11.50	0.63	−11.79	0.53	6.3	0
NGVS J12:26:27.83+12:45:52.7	−9.14	0.59	−10.22	0.28	−10.81	0.22	−11.26	0.56	−11.20	0.54	6.2	0
NGVS J12:26:28.06+12:55:14.2	−13.16	0.23	−14.19	0.11	−14.84	0.10	−15.16	0.17	−16.02	0.01	7.9	1
NGVS J12:26:31.31+12:29:32.4	−8.24	0.42	−9.11	0.34	−9.64	0.36	−10.29	1.12	−11.16	0.41	5.8	0
NGVS J12:26:32.25+12:36:38.5	−17.47	0.23	−18.58	0.02	−19.28	0.01	−19.57	0.01	−19.77	0.02	9.8	0
NGVS J12:26:32.68+13:25:25.8	−10.16	0.24	−10.94	0.11	−11.61	0.15	−11.73	0.19	−12.22	0.28	6.4	0
NGVS J12:26:33.21+12:44:34.7	−13.98	0.23	−15.48	0.11	−16.18	0.10	−16.55	0.17	−16.81	0.19	8.5	1
NGVS J12:26:35.84+13:22:44.7	−8.95	0.33	−9.76	0.28	−10.48	0.28	−10.84	0.43	−11.51	0.85	6.0	0
NGVS J12:26:36.32+12:48:10.0	−12.38	0.16	−13.20	0.07	−13.76	0.07	−14.00	0.11	−14.18	0.13	7.4	1
NGVS J12:26:37.74+12:43:48.1	−7.85	0.94	−8.67	0.34	−9.14	0.30	−9.43	0.77	−9.48	1.42	5.3	0
NGVS J12:26:38.09+11:53:30.7	−10.65	0.40	−11.62	0.13	−12.17	0.13	−12.37	0.19	−12.34	0.53	6.7	1
NGVS J12:26:38.25+13:04:44.2	−11.68	0.60	−12.90	0.48	−13.41	0.47	−13.71	0.68	−13.96	0.19	7.2	1
NGVS J12:26:39.81+12:30:48.8	−14.01	0.01	−15.18	0.11	−15.76	0.10	−16.02	0.17	−16.11	0.19	8.2	1
NGVS J12:26:41.15+12:50:43.5	−12.03	0.09	−13.11	0.04	−13.61	0.05	−14.03	0.06	−14.14	0.09	7.4	0
NGVS J12:26:42.11+13:22:33.3	−7.49	0.23	−9.19	0.11	−9.41	0.10	−9.91	0.17	−10.28	0.19	5.6	0
NGVS J12:26:43.31+12:17:44.0	−11.73	0.10	−12.70	0.15	−13.13	0.09	−13.48	0.17	−13.65	0.19	7.1	1
NGVS J12:26:44.62+13:11:16.4	−8.32	0.24	−9.11	0.31	−9.57	0.28	−9.79	0.55	−9.87	0.19	5.5	0
NGVS J12:26:46.58+13:16:00.6	−11.21	0.24	−12.16	0.08	−13.08	0.09	−13.28	0.14	−15.13	0.19	7.1	0
NGVS J12:26:46.70+11:41:55.1	−8.33	0.23	−8.61	0.52	−9.05	0.50	−9.34	0.17	−9.91	0.19	5.3	0
NGVS J12:26:47.06+12:27:14.3	−15.47	0.01	−16.61	0.11	−17.27	0.10	−17.61	0.17	−17.77	0.01	8.9	1
NGVS J12:26:47.88+13:22:44.9	−11.44	0.04	−12.46	0.02	−13.01	0.01	−13.23	0.03	−13.39	0.04	7.0	0
NGVS J12:26:48.25+12:31:35.8	−10.25	0.74	−10.96	0.26	−11.54	0.23	−11.94	0.54	−12.24	0.61	6.5	0
NGVS J12:26:48.36+13:21:17.7	−10.27	0.41	−12.12	0.60	−12.38	0.31	−12.77	0.61	−12.53	0.67	6.8	0
NGVS J12:26:48.49+12:23:59.6	−10.74	0.14	−11.57	0.04	−12.01	0.04	−12.31	0.08	−12.40	0.19	6.7	0
NGVS J12:26:49.16+12:18:38.1	−8.30	0.41	−9.39	0.42	−9.74	0.42	−10.20	0.52	−10.13	0.19	5.7	0
NGVS J12:26:49.59+12:10:43.0	−9.70	0.28	−10.72	0.07	−11.27	0.12	−11.50	0.13	−11.54	0.61	6.3	0
NGVS J12:26:50.74+11:33:27.5	−15.41	0.06	−16.04	0.06	−16.26	0.06	−16.41	0.06	−16.89	0.08	8.4	0
NGVS J12:26:50.83+13:10:36.9	−15.31	0.08	−15.87	0.09	−16.15	0.09	−16.27	0.09	−16.41	0.10	8.4	0
NGVS J12:26:51.99+12:39:08.2	−9.50	0.29	−10.55	0.23	−11.08	0.21	−11.39	0.39	−11.11	0.47	6.3	1
NGVS J12:26:54.36+11:39:50.2	−16.09	0.01	−17.17	0.11	−17.70	0.10	−17.96	0.17	−18.04	0.01	9.1	1
NGVS J12:26:55.15+12:43:13.6	−8.64	0.29	−9.63	0.83	−10.08	0.89	−10.40	0.73	−10.23	1.27	5.8	0
NGVS J12:26:55.63+12:51:33.6	−9.32	0.29	−10.26	0.17	−10.70	0.14	−10.82	0.24	−10.95	0.47	6.0	0
NGVS J12:26:55.95+12:59:40.0	−10.86	0.35	−11.88	0.21	−12.85	0.16	−13.03	0.73	−13.20	0.43	7.0	0
NGVS J12:26:56.47+12:57:43.3	−11.66	0.20	−12.47	0.06	−13.00	0.07	−13.29	0.11	−13.46	0.16	7.1	0
NGVS J12:26:56.67+11:36:12.6	−7.68	1.07	−8.73	0.34	−9.29	0.40	−9.35	0.63	−9.34	0.75	5.3	0
NGVS J12:26:57.65+12:25:16.2	−9.72	0.26	−11.06	0.08	−11.65	0.07	−11.88	0.12	−11.99	0.19	6.5	0
NGVS J12:26:58.93+12:33:13.5	−7.91	0.23	−9.99	0.88	−10.45	0.94	−10.35	0.88	−11.90	0.81	5.8	0
NGVS J12:26:59.05+12:30:20.5	−13.27	0.07	−14.24	0.03	−14.91	0.03	−15.13	0.04	−15.36	0.06	7.9	0
NGVS J12:27:02.60+12:34:47.1	−11.34	0.37	−12.39	0.16	−13.11	0.15	−13.39	0.18	−13.59	0.27	7.1	0
NGVS J12:27:03.08+12:33:38.8	−14.82	0.02	−15.96	0.11	−16.56	0.01	−16.82	0.01	−16.98	0.01	8.6	1
NGVS J12:27:03.76+11:31:51.0	−9.12	0.23	−10.00	0.47	−10.22	0.47	−10.66	0.84	−11.61	1.23	5.9	0
NGVS J12:27:03.81+12:51:59.2	−11.72	0.08	−12.79	0.04	−13.45	0.05	−13.66	0.06	−13.87	0.10	7.2	0
NGVS J12:27:06.07+13:19:25.3	−11.95	0.05	−12.86	0.03	−13.36	0.03	−13.57	0.04	−13.77	0.06	7.2	0
NGVS J12:27:08.42+13:20:08.7	−13.62	0.06	−14.72	0.01	−15.29	0.02	−15.52	0.03	−15.58	0.03	8.0	1
NGVS J12:27:10.65+12:46:03.6	−9.30	0.23	−9.22	0.28	−9.81	0.73	−10.16	0.10	−10.41	0.19	5.7	0
NGVS J12:27:11.20+12:06:52.3	−12.16	0.09	−13.17	0.06	−13.67	0.05	−14.00	0.06	−13.68	0.19	7.4	1
NGVS J12:27:11.24+12:02:17.4	−12.22	0.04	−13.26	0.11	−13.82	0.01	−14.17	0.17	−14.10	0.05	7.4	1
NGVS J12:27:12.75+13:13:14.6	−9.31	0.47	−10.28	0.12	−10.80	0.13	−10.99	0.25	−10.87	0.35	6.1	0
NGVS J12:27:13.34+12:44:05.2	−17.48	0.23	−18.79	0.11	−19.43	0.10	−19.78	0.17	−19.99	0.19	9.9	1
NGVS J12:27:14.21+12:54:09.6	−10.00	0.53	−10.67	0.17	−11.19	0.10	−11.41	0.17	−11.97	0.81	6.3	0
NGVS J12:27:15.01+12:50:55.9	−12.11	0.23	−12.11	0.48	−12.87	0.40	−11.61	0.46	−11.81	0.51	6.4	0
NGVS J12:27:15.46+12:39:41.4	−12.58	0.63	−13.05	0.12	−13.75	0.10	−13.70	0.11	−14.58	0.24	7.2	0
NGVS J12:27:15.46+13:24:44.8	−10.52	0.58	−11.41	0.22	−11.83	0.15	−12.07	0.28	−11.96	0.39	6.6	0
NGVS J12:27:16.78+12:32:07.8	−8.81	0.23	−9.82	0.11	−10.34	0.06	−10.51	0.18	−10.52	0.45	5.9	1
NGVS J12:27:19.52+12:13:15.9	−10.50	0.30	−11.48	0.15	−12.20	0.19	−12.45	0.27	−12.83	0.83	6.7	0
NGVS J12:27:19.62+13:05:13.3	−9.32	0.27	−10.32	0.12	−10.88	0.11	−11.16	0.25	−11.05	0.35	6.2	0
NGVS J12:27:20.29+11:41:42.8	−9.56	0.23	−10.56	0.11	−11.11	0.10	−11.87	0.26	−11.78	0.49	6.5	0
NGVS J12:27:21.11+13:06:40.3	−12.13	0.07	−13.12	0.04	−13.70	0.04	−13.91	0.06	−14.07	0.09	7.3	0

Table 4
(Continued)

ID	M_u	Δu	M_g	Δg	M_r	Δr	M_i	Δi	M_z	Δz	log ($M_*/M_\odot$)	Nucleation
NGVS J12:27:22.17+12:04:07.4	−12.68	0.06	−13.57	0.02	−14.11	0.02	−14.33	0.03	−14.38	0.05	7.5	1
NGVS J12:27:23.46+12:19:54.1	−12.45	0.08	−13.41	0.03	−13.95	0.03	−14.23	0.04	−14.13	0.09	7.5	1
NGVS J12:27:25.10+13:24:21.9	−11.14	0.34	−12.26	0.09	−12.81	0.09	−13.00	0.13	−13.08	0.25	6.9	0
NGVS J12:27:26.91+11:45:11.6	−7.68	1.07	−9.12	0.87	−9.48	0.77	−9.32	1.40	−9.83	0.59	5.3	0
NGVS J12:27:26.95+11:56:33.4	−10.13	0.24	−11.06	0.08	−11.55	0.06	−11.77	0.10	−11.70	0.26	6.4	0
NGVS J12:27:27.38+12:17:25.0	−16.47	0.23	−17.73	0.11	−18.39	0.10	−18.74	0.17	−18.91	0.01	9.4	0
NGVS J12:27:29.53+12:16:09.1	−9.92	0.33	−11.05	0.11	−11.68	0.14	−11.97	0.21	−13.82	0.83	6.5	0
NGVS J12:27:29.55+11:44:04.1	−9.33	0.36	−10.51	0.13	−11.02	0.10	−11.37	0.22	−11.79	0.37	6.3	0
NGVS J12:27:29.78+12:15:07.2	−11.42	0.23	−12.25	0.11	−12.60	0.11	−12.96	0.18	−12.24	0.19	6.9	1
NGVS J12:27:30.38+13:12:55.1	−8.91	1.05	−9.38	0.34	−9.79	0.31	−10.02	0.47	−10.62	0.33	5.6	0
NGVS J12:27:32.01+11:36:54.7	−13.01	0.03	−14.11	0.01	−14.69	0.01	−14.93	0.02	−15.07	0.04	7.8	1
NGVS J12:27:33.11+11:31:43.3	−8.43	0.96	−9.66	0.24	−10.28	0.23	−10.68	0.41	−11.02	0.19	5.9	0
NGVS J12:27:33.18+11:31:55.7	−10.80	0.40	−11.57	0.12	−12.08	0.12	−12.35	0.18	−12.19	0.19	6.7	1
NGVS J12:27:34.39+12:48:12.1	−10.23	0.51	−11.68	0.19	−12.67	0.21	−12.60	0.32	−13.32	0.19	6.8	0
NGVS J12:27:35.60+12:37:26.3	−11.07	0.54	−12.06	0.17	−12.60	0.20	−13.01	0.26	−12.88	0.33	6.9	0
NGVS J12:27:37.45+12:22:40.9	−8.32	1.11	−8.93	0.49	−9.39	0.47	−9.57	0.64	−10.60	1.20	5.4	0
NGVS J12:27:39.24+12:52:47.6	−12.89	0.11	−13.80	0.04	−14.33	0.04	−14.50	0.06	−14.98	0.10	7.6	1
NGVS J12:27:40.49+13:04:44.3	−18.79	0.23	−20.09	0.11	−20.78	0.10	−21.10	0.17	−21.31	0.19	10.5	1
NGVS J12:27:41.24+12:18:57.2	−16.26	0.23	−17.52	0.11	−18.13	0.10	−18.44	0.17	−18.59	0.19	9.3	1
NGVS J12:27:41.67+12:29:16.3	−10.47	0.20	−11.39	0.07	−11.94	0.06	−12.10	0.11	−12.19	0.15	6.6	0
NGVS J12:27:42.11+12:05:22.7	−13.95	0.02	−14.88	0.11	−15.33	0.01	−15.71	0.01	−15.73	0.02	8.1	0
NGVS J12:27:43.43+11:58:04.6	−10.05	0.23	−11.26	0.11	−11.79	0.10	−11.92	0.17	−12.14	0.40	6.5	0
NGVS J12:27:44.39+12:33:25.9	−9.27	0.76	−10.66	0.26	−11.06	0.16	−11.15	0.32	−11.52	0.46	6.2	0
NGVS J12:27:44.52+12:59:01.3	−14.58	0.07	−15.67	0.03	−16.37	0.03	−16.56	0.03	−16.78	0.04	8.5	1
NGVS J12:27:45.42+12:52:22.5	−12.22	0.09	−13.06	0.03	−13.58	0.04	−13.72	0.06	−13.90	0.09	7.3	0
NGVS J12:27:45.65+13:00:31.9	−19.13	0.11	−20.17	0.07	−20.72	0.10	−21.21	0.04	−21.65	0.19	10.5	0
NGVS J12:27:46.47+11:44:28.9	−10.41	0.23	−11.57	0.08	−12.11	0.09	−12.36	0.13	−12.39	0.26	6.7	0
NGVS J12:27:49.49+12:29:58.7	−10.63	0.23	−11.52	0.09	−12.05	0.09	−12.32	0.16	−12.57	0.26	6.7	0
NGVS J12:27:53.17+12:22:58.8	−9.44	0.41	−10.31	0.15	−10.84	0.19	−11.08	0.25	−11.46	0.76	6.1	0
NGVS J12:27:53.42+12:58:22.9	−8.47	0.79	−9.15	0.27	−9.73	0.35	−9.88	0.17	−9.71	0.19	5.6	0
NGVS J12:27:53.57+12:17:35.8	−17.51	0.23	−18.74	0.11	−19.52	0.10	−19.87	0.17	−20.32	0.19	9.9	1
NGVS J12:27:54.56+12:36:16.2	−10.58	0.14	−11.52	0.07	−12.06	0.07	−12.27	0.10	−12.46	0.15	6.6	0
NGVS J12:27:55.22+12:22:09.5	−14.10	0.27	−15.03	0.08	−15.54	0.07	−15.85	0.12	−15.50	0.22	8.2	0
NGVS J12:28:00.33+11:30:34.7	−9.75	0.45	−10.68	0.12	−11.27	0.12	−11.70	0.20	−11.95	0.33	6.4	0
NGVS J12:28:00.44+11:56:59.6	−12.30	0.04	−13.39	0.01	−13.94	0.01	−14.23	0.02	−14.39	0.04	7.5	1
NGVS J12:28:03.74+12:46:41.2	−9.09	0.44	−10.05	0.06	−10.62	0.17	−10.79	0.27	−10.50	0.56	6.0	1
NGVS J12:28:04.79+11:36:16.5	−10.60	0.24	−11.71	0.12	−12.19	0.11	−12.48	0.15	−12.62	0.35	6.7	0
NGVS J12:28:05.92+12:50:15.5	−9.67	0.21	−10.71	0.07	−11.24	0.07	−11.45	0.10	−11.49	0.19	6.3	0
NGVS J12:28:06.53+12:53:53.3	−13.70	0.01	−14.80	0.01	−15.37	0.10	−15.63	0.01	−15.76	0.02	8.1	1
NGVS J12:28:06.77+12:58:43.2	−11.00	0.23	−12.11	0.12	−12.61	0.12	−13.02	0.19	−13.27	0.24	7.0	1
NGVS J12:28:07.90+12:24:07.9	−8.76	0.59	−9.92	0.17	−10.33	0.14	−10.49	0.25	−10.50	0.19	5.9	0
NGVS J12:28:08.61+12:05:35.8	−15.77	0.02	−16.98	0.01	−17.55	0.02	−18.00	0.01	−18.11	0.02	9.1	1
NGVS J12:28:10.07+12:43:29.4	−11.74	0.30	−12.67	0.20	−12.88	0.24	−13.07	0.27	−13.32	0.25	7.0	0
NGVS J12:28:10.28+12:48:32.2	−11.45	0.08	−12.20	0.04	−12.75	0.05	−12.86	0.12	−13.24	0.18	6.9	1
NGVS J12:28:12.24+11:58:13.3	−10.60	0.16	−11.75	0.04	−12.25	0.06	−12.53	0.09	−12.55	0.26	6.7	1
NGVS J12:28:12.60+12:45:33.9	−8.38	1.43	−9.21	0.42	−9.71	0.33	−9.68	0.57	−10.25	0.26	5.5	0
NGVS J12:28:12.81+13:00:54.0	−11.09	0.10	−12.12	0.04	−12.61	0.04	−12.84	0.07	−12.82	0.12	6.9	0
NGVS J12:28:12.86+12:54:56.5	−7.77	1.07	−8.72	0.40	−9.02	0.39	−9.30	0.37	−10.37	1.21	5.3	0
NGVS J12:28:14.87+11:47:23.6	−16.22	0.01	−17.95	0.11	−18.39	0.10	−18.74	0.17	−18.77	0.19	9.4	1
NGVS J12:28:15.41+12:33:37.2	−8.65	0.29	−9.78	0.17	−10.50	0.17	−11.08	0.33	−11.52	0.45	6.1	0
NGVS J12:28:18.74+11:42:00.9	−13.65	0.04	−14.84	0.02	−15.55	0.03	−15.68	0.03	−15.90	0.06	8.1	1
NGVS J12:28:20.08+13:18:37.2	−8.31	0.74	−8.33	1.33	−8.55	0.32	−9.77	0.90	−8.90	0.19	5.5	0
NGVS J12:28:20.18+13:21:35.5	−9.62	1.03	−10.40	0.36	−10.95	0.28	−11.03	0.45	−10.90	0.19	6.1	0
NGVS J12:28:21.59+12:38:45.4	−8.42	0.23	−9.44	0.32	−9.87	0.25	−10.16	0.62	−10.64	0.34	5.7	0
NGVS J12:28:21.66+12:08:04.0	−11.16	0.71	−12.22	0.37	−13.47	0.38	−13.30	0.48	−13.93	0.56	7.1	1
NGVS J12:28:23.37+11:34:46.9	−12.17	0.06	−13.15	0.02	−13.69	0.03	−13.86	0.04	−14.05	0.10	7.3	0
NGVS J12:28:23.64+13:11:44.7	−14.12	0.02	−15.27	0.01	−15.80	0.10	−16.05	0.02	−16.22	0.02	8.3	1
NGVS J12:28:26.26+12:20:45.2	−11.20	0.23	−12.21	0.11	−12.76	0.10	−12.96	0.24	−13.15	0.50	6.9	1
NGVS J12:28:27.72+12:33:29.9	−8.56	0.97	−8.98	0.47	−9.67	0.38	−9.67	0.67	−9.45	0.19	5.5	0
NGVS J12:28:28.06+12:49:25.3	−14.83	0.01	−15.96	0.11	−16.53	0.10	−16.73	0.17	−16.87	0.19	8.6	1
NGVS J12:28:29.72+11:58:19.6	−9.25	0.35	−10.17	0.13	−10.65	0.13	−10.83	0.19	−10.93	0.19	6.0	0
NGVS J12:28:31.15+11:31:59.9	−8.97	0.85	−9.70	0.28	−10.19	0.24	−10.53	0.49	−10.31	0.19	5.9	0
NGVS J12:28:31.99+12:59:16.6	−9.63	0.96	−9.57	0.29	−10.04	0.32	−10.32	0.17	−8.93	0.19	5.8	0
NGVS J12:28:32.13+12:32:09.7	−8.40	0.50	−9.07	0.77	−9.40	0.45	−8.87	0.79	−8.95	0.19	5.1	0
NGVS J12:28:32.40+11:44:40.7	−13.53	0.16	−14.08	0.06	−14.61	0.10	−14.80	0.17	−15.24	0.13	7.7	1

Table 4
(Continued)

ID	M_u	Δu	M_g	Δg	M_r	Δr	M_i	Δi	M_z	Δz	log ($M_*/M_\odot$)	Nucleation
NGVS J12:28:35.75+12:10:57.2	−7.76	0.23	−8.69	0.28	−9.18	0.27	−9.52	0.64	−9.81	0.19	5.4	0
NGVS J12:28:36.07+11:40:16.5	−8.31	0.45	−9.31	0.23	−9.68	0.20	−10.18	0.36	−10.27	1.00	5.7	0
NGVS J12:28:39.87+12:58:40.5	−10.05	0.62	−10.94	0.15	−11.55	0.15	−11.58	0.26	−12.00	0.53	6.3	0
NGVS J12:28:41.71+12:54:57.2	−15.39	0.23	−16.50	0.11	−17.04	0.10	−17.30	0.17	−17.46	0.19	8.8	1
NGVS J12:28:42.66+12:32:59.4	−13.68	0.06	−14.69	0.02	−15.29	0.02	−15.53	0.03	−15.64	0.03	8.0	1
NGVS J12:28:43.31+11:45:18.1	−17.45	0.23	−18.71	0.10	−19.25	0.01	−19.70	0.01	−19.93	0.02	9.9	0
NGVS J12:28:44.65+11:59:37.2	−9.22	0.26	−10.15	0.07	−10.56	0.07	−10.89	0.13	−10.85	0.26	6.0	0
NGVS J12:28:44.91+12:48:34.3	−12.53	0.03	−13.54	0.01	−14.06	0.01	−14.28	0.02	−14.42	0.03	7.5	0
NGVS J12:28:45.79+12:01:18.6	−12.40	0.10	−13.29	0.03	−13.88	0.04	−14.05	0.05	−13.98	0.15	7.4	0
NGVS J12:28:46.92+12:38:31.5	−10.31	0.89	−11.15	0.14	−11.79	0.06	−11.97	0.23	−12.01	0.30	6.5	1
NGVS J12:28:47.37+12:49:48.5	−7.52	1.08	−8.59	0.41	−9.66	0.56	−9.20	0.29	−9.01	0.53	5.2	0
NGVS J12:28:48.93+11:53:10.4	−8.59	1.04	−9.64	0.30	−10.17	0.28	−10.51	0.42	−10.23	0.58	5.9	0
NGVS J12:28:49.11+12:07:54.5	−11.77	0.10	−12.71	0.03	−13.28	0.10	−13.38	0.07	−13.52	0.14	7.1	0
NGVS J12:28:49.98+12:47:46.7	−10.69	0.09	−11.59	0.03	−12.13	0.03	−12.34	0.05	−12.47	0.08	6.7	0
NGVS J12:28:51.02+12:07:09.0	−8.87	0.17	−9.69	0.71	−10.03	0.80	−10.28	0.88	−10.24	0.57	5.8	0
NGVS J12:28:51.07+11:34:24.8	−9.56	0.46	−10.50	0.18	−10.95	0.15	−11.12	0.23	−11.46	0.20	6.1	0
NGVS J12:28:51.30+11:57:26.9	−10.38	0.19	−11.52	0.07	−12.11	0.09	−12.14	0.15	−12.00	0.19	6.6	0
NGVS J12:28:52.76+12:44:12.3	−9.60	0.38	−10.63	0.28	−11.40	0.25	−11.58	0.54	−11.33	0.36	6.3	0
NGVS J12:28:53.71+13:11:51.2	−8.91	0.29	−10.07	0.14	−10.52	0.15	−10.80	0.33	−10.90	0.60	6.0	0
NGVS J12:28:53.73+12:58:53.7	−9.09	0.41	−9.95	0.16	−10.32	0.14	−10.59	0.21	−10.95	0.39	5.9	0
NGVS J12:28:55.57+12:42:24.6	−11.50	0.12	−12.38	0.04	−12.86	0.04	−13.15	0.06	−13.37	0.09	7.0	0
NGVS J12:28:55.65+12:25:42.3	−9.00	0.23	−9.64	0.36	−9.96	0.39	−10.65	0.50	−10.76	0.19	5.9	0
NGVS J12:28:56.04+12:42:54.8	−7.37	0.23	−8.81	0.11	−9.53	0.55	−9.49	1.41	−9.23	0.31	5.4	0
NGVS J12:28:56.13+13:26:42.2	−10.61	0.68	−11.25	0.15	−11.61	0.17	−11.86	0.47	−13.05	0.17	6.5	0
NGVS J12:28:57.56+13:14:31.0	−17.52	0.03	−18.71	0.01	−19.38	0.01	−19.68	0.01	−19.92	0.02	9.8	0
NGVS J12:28:57.68+11:57:20.2	−9.93	0.25	−11.08	0.10	−11.62	0.06	−11.85	0.12	−11.55	0.34	6.5	1
NGVS J12:28:58.14+12:39:42.2	−13.91	0.04	−15.44	0.01	−16.18	0.02	−16.54	0.01	−16.80	0.02	8.5	1
NGVS J12:28:58.84+12:54:28.8	−13.03	0.14	−13.76	0.04	−14.23	0.05	−14.45	0.10	−14.41	0.13	7.6	0
NGVS J12:28:59.15+12:02:30.4	−10.07	0.26	−10.68	0.30	−11.33	0.38	−11.50	0.42	−10.86	1.34	6.3	1
NGVS J12:28:59.50+11:55:23.4	−11.02	0.36	−11.62	0.35	−12.13	0.33	−12.75	0.96	−10.12	1.20	6.8	1
NGVS J12:28:59.82+12:38:54.2	−12.38	0.06	−13.62	0.02	−14.18	0.02	−14.53	0.03	−14.60	0.06	7.6	1
NGVS J12:29:01.16+12:33:30.8	−8.68	0.51	−9.68	0.19	−10.28	0.18	−10.52	0.35	−10.89	0.80	5.9	0
NGVS J12:29:01.17+12:25:50.2	−7.07	0.49	−8.09	0.48	−8.51	0.39	−8.91	0.26	−8.88	0.47	5.1	0
NGVS J12:29:02.02+12:26:05.5	−10.74	0.21	−11.87	0.07	−12.40	0.07	−12.55	0.10	−12.91	0.26	6.8	0
NGVS J12:29:03.01+13:11:01.7	−18.11	0.23	−19.54	0.01	−20.24	0.10	−20.59	0.17	−20.81	0.19	10.2	1
NGVS J12:29:03.26+12:05:58.9	−8.37	0.81	−8.91	0.80	−9.72	0.73	−9.39	0.17	−9.70	0.31	5.3	0
NGVS J12:29:05.13+12:09:13.6	−10.65	0.18	−11.71	0.16	−12.19	0.17	−12.57	0.25	−13.42	0.19	6.8	1
NGVS J12:29:05.42+12:01:52.5	−11.07	0.11	−12.16	0.04	−12.74	0.07	−12.91	0.06	−12.83	0.19	6.9	0
NGVS J12:29:09.24+12:29:45.6	−9.38	0.23	−10.71	0.17	−11.23	0.15	−11.30	0.24	−11.32	0.29	6.2	0
NGVS J12:29:09.56+12:33:29.3	−7.32	0.79	−10.55	0.12	−10.63	0.16	−11.33	0.43	−10.44	0.19	6.2	0
NGVS J12:29:11.82+13:09:48.7	−10.11	0.58	−11.09	0.11	−11.94	0.27	−12.18	0.26	−12.64	0.39	6.6	0
NGVS J12:29:12.31+11:31:11.9	−9.11	0.48	−10.40	0.14	−10.80	0.10	−11.09	0.16	−10.64	0.19	6.1	1
NGVS J12:29:14.85+12:58:41.7	−13.98	0.01	−15.18	0.11	−15.74	0.10	−16.00	0.17	−16.13	0.01	8.2	1
NGVS J12:29:17.55+13:04:42.6	−9.32	0.23	−10.14	0.30	−10.32	0.15	−10.34	1.35	−10.95	0.19	5.8	0
NGVS J12:29:19.28+12:22:37.2	−11.96	0.23	−12.89	0.11	−13.47	0.10	−13.73	0.17	−13.98	0.19	7.3	0
NGVS J12:29:20.27+12:01:16.4	−11.50	0.23	−12.51	0.08	−13.12	0.24	−13.40	0.17	−13.40	0.19	7.1	0
NGVS J12:29:20.73+13:22:12.0	−8.74	0.54	−10.13	0.31	−10.50	0.32	−10.56	0.63	−10.35	0.19	5.9	0
NGVS J12:29:21.55+12:28:03.4	−9.89	0.34	−10.17	0.18	−10.66	0.16	−10.74	0.31	−11.57	0.19	6.0	0
NGVS J12:29:22.40+11:49:17.7	−8.28	0.89	−9.53	0.28	−10.08	0.26	−10.13	0.38	−9.98	0.41	5.7	0
NGVS J12:29:23.52+12:27:02.9	−14.70	0.03	−15.98	0.11	−16.54	0.10	−16.82	0.01	−17.03	0.01	8.6	1
NGVS J12:29:26.27+13:06:50.3	−7.84	0.21	−8.64	0.95	−9.26	0.69	−9.60	1.12	−6.65	0.24	5.4	0
NGVS J12:29:28.67+12:29:46.3	−12.74	0.06	−13.76	0.02	−14.30	0.02	−14.43	0.04	−14.69	0.06	7.5	1
NGVS J12:29:31.38+12:34:12.1	−10.77	0.07	−11.86	0.02	−12.37	0.02	−12.57	0.04	−12.68	0.06	6.8	0
NGVS J12:29:33.61+13:11:44.6	−12.13	0.05	−12.89	0.04	−13.22	0.03	−13.29	0.04	−13.39	0.05	7.1	0
NGVS J12:29:34.52+13:19:56.2	−11.59	0.08	−12.77	0.03	−13.33	0.03	−13.61	0.05	−13.81	0.08	7.2	0
NGVS J12:29:35.56+12:03:36.0	−7.47	0.23	−9.31	0.69	−9.21	0.79	−9.87	1.12	−9.01	0.19	5.6	0
NGVS J12:29:35.57+13:12:40.1	−8.88	0.47	−10.38	0.15	−10.88	0.16	−11.04	0.24	−11.45	0.45	6.1	0
NGVS J12:29:38.10+13:05:18.2	−8.97	0.44	−10.20	0.74	−10.55	0.16	−10.89	0.79	−9.48	0.88	6.0	0
NGVS J12:29:38.15+12:24:35.5	−9.49	0.20	−10.79	0.29	−11.26	0.22	−11.41	0.29	−10.82	0.40	6.3	0
NGVS J12:29:39.06+11:38:00.3	−13.32	0.11	−14.34	0.04	−14.84	0.04	−15.21	0.05	−15.23	0.14	7.9	1
NGVS J12:29:39.24+12:32:53.7	−13.92	0.04	−15.08	0.01	−15.63	0.01	−15.89	0.02	−16.10	0.03	8.2	1
NGVS J12:29:39.32+12:25:00.3	−8.96	0.85	−9.77	0.14	−10.31	0.14	−10.48	0.22	−11.25	0.58	5.8	0
NGVS J12:29:39.65+12:14:15.8	−11.19	0.86	−11.19	0.29	−11.64	0.15	−12.06	0.22	−12.10	0.76	6.5	0
NGVS J12:29:39.70+11:52:05.2	−9.25	0.25	−10.24	0.10	−10.77	0.11	−11.11	0.17	−11.10	0.19	6.1	0
NGVS J12:29:40.38+12:57:38.5	−9.06	0.25	−9.87	0.30	−10.59	0.33	−10.58	0.53	−11.06	0.30	5.9	0

Table 4
(Continued)

ID	M_u	Δu	M_g	Δg	M_r	Δr	M_i	Δi	M_z	Δz	log ($M_*/M_\odot$)	Nucleation
NGVS J12:29:41.28+12:02:45.9	−11.72	0.15	−12.87	0.04	−13.43	0.06	−13.63	0.07	−13.61	0.19	7.2	1
NGVS J12:29:41.39+11:34:19.3	−10.22	0.45	−11.37	0.18	−11.73	0.13	−12.12	0.22	−12.03	0.52	6.6	1
NGVS J12:29:41.52+12:29:56.9	−8.61	0.38	−9.88	0.22	−10.17	0.20	−10.28	0.34	−10.59	0.41	5.8	0
NGVS J12:29:43.19+12:39:18.8	−8.91	0.42	−10.16	0.11	−10.55	0.24	−10.76	0.26	−11.12	0.43	6.0	0
NGVS J12:29:44.09+12:48:19.6	−12.23	0.06	−13.07	0.02	−13.63	0.02	−13.78	0.04	−13.93	0.03	7.3	1
NGVS J12:29:46.27+12:55:27.8	−9.33	1.06	−10.41	0.29	−10.89	0.31	−11.23	0.64	−11.24	0.88	6.2	0
NGVS J12:29:47.20+13:04:34.4	−10.75	0.10	−11.81	0.04	−12.35	0.02	−12.54	0.04	−12.65	0.19	6.8	0
NGVS J12:29:47.74+12:34:17.2	−8.04	0.67	−9.26	0.41	−9.28	0.32	−9.82	1.13	−8.04	0.19	5.5	0
NGVS J12:29:48.87+13:25:46.0	−19.23	0.23	−20.54	0.01	−21.24	0.02	−21.59	0.02	−21.86	0.01	10.7	0
NGVS J12:29:50.47+12:04:42.5	−7.21	0.23	−8.62	0.51	−9.04	0.36	−9.22	0.52	−9.88	0.17	5.2	0
NGVS J12:29:52.01+13:19:28.0	−9.70	0.22	−10.84	0.11	−11.29	0.09	−11.58	0.18	−11.76	0.32	6.3	0
NGVS J12:29:53.00+11:57:44.3	−14.26	0.12	−14.25	0.03	−14.73	0.04	−14.92	0.05	−14.96	0.08	7.8	1
NGVS J12:29:53.78+12:37:17.9	−11.23	0.23	−12.20	0.21	−12.63	0.21	−12.92	0.28	−13.27	0.39	6.9	0
NGVS J12:29:54.77+12:55:51.4	−7.37	0.96	−9.16	0.26	−9.56	0.26	−9.60	0.86	−9.36	0.12	5.4	0
NGVS J12:29:55.50+13:20:58.2	−9.12	0.60	−9.87	0.24	−10.37	0.22	−10.59	0.45	−10.45	0.56	5.9	0
NGVS J12:29:56.24+12:40:17.4	−8.06	0.53	−9.46	0.41	−9.47	0.36	−9.86	0.70	−9.95	1.18	5.6	0
NGVS J12:29:56.34+13:13:12.3	−12.33	0.50	−13.39	0.10	−14.32	0.17	−14.12	0.17	−14.78	0.35	7.4	1
NGVS J12:29:58.26+13:16:20.8	−11.56	0.10	−12.61	0.03	−13.09	0.04	−13.29	0.07	−13.35	0.10	7.1	1
NGVS J12:29:58.67+11:54:42.5	−7.11	0.23	−8.87	0.11	−8.90	0.10	−10.19	0.50	−9.10	0.19	5.7	0
NGVS J12:29:59.08+12:20:55.4	−17.40	0.23	−18.53	0.11	−19.20	0.10	−19.54	0.17	−19.91	0.19	9.8	1
NGVS J12:30:00.94+12:44:11.3	−8.19	0.39	−9.54	0.51	−9.86	0.45	−10.14	0.74	−10.45	0.47	5.7	0
NGVS J12:30:01.15+13:07:04.9	−10.35	0.21	−11.53	0.03	−12.05	0.10	−12.18	0.19	−12.41	0.19	6.6	1
NGVS J12:30:01.82+12:56:52.5	−9.43	0.24	−10.55	0.09	−11.01	0.10	−11.20	0.14	−11.28	0.19	6.2	0
NGVS J12:30:01.87+12:12:59.7	−9.43	0.21	−10.60	0.15	−11.00	0.13	−11.35	0.16	−11.24	0.19	6.2	0
NGVS J12:30:04.38+12:30:35.7	−8.29	0.35	−9.46	0.14	−9.98	0.17	−10.18	0.29	−10.28	0.60	5.7	0
NGVS J12:30:05.12+12:38:48.7	−7.86	1.36	−8.65	0.59	−9.02	0.47	−9.54	1.39	−8.69	0.86	5.4	0
NGVS J12:30:05.91+12:27:12.1	−6.93	0.23	−8.43	0.52	−8.85	0.72	−9.21	1.35	−8.26	0.19	5.2	0
NGVS J12:30:06.08+12:22:37.9	−12.13	0.06	−13.23	0.02	−13.69	0.03	−13.94	0.04	−14.04	0.08	7.3	0
NGVS J12:30:06.21+12:41:18.4	−11.36	0.30	−12.35	0.08	−12.76	0.07	−12.96	0.17	−13.15	0.14	6.9	1
NGVS J12:30:07.20+12:35:28.2	−8.55	0.58	−8.96	0.62	−8.85	1.04	−9.34	1.35	−9.31	1.24	5.3	0
NGVS J12:30:07.86+12:23:19.9	−9.50	0.19	−10.60	0.06	−11.08	0.05	−11.20	0.10	−11.50	0.21	6.2	1
NGVS J12:30:10.88+12:11:43.6	−13.71	0.07	−14.70	0.03	−15.16	0.03	−15.45	0.04	−15.42	0.07	8.0	1
NGVS J12:30:13.90+12:56:48.8	−8.60	0.23	−9.72	1.02	−11.48	0.10	−11.58	0.17	−10.27	0.19	6.3	0
NGVS J12:30:15.05+13:20:31.0	−8.28	0.23	−9.55	0.64	−9.98	0.31	−9.97	0.17	−10.55	0.19	5.6	0
NGVS J12:30:15.27+12:30:57.3	−11.07	0.23	−12.02	0.06	−12.44	0.06	−12.68	0.09	−12.82	0.19	6.8	0
NGVS J12:30:15.76+12:59:54.0	−9.12	0.49	−10.07	0.24	−10.60	0.21	−10.95	0.30	−11.22	0.39	6.1	0
NGVS J12:30:15.99+13:18:27.6	−11.02	0.09	−12.05	0.03	−12.55	0.01	−12.81	0.17	−12.85	0.10	6.9	1
NGVS J12:30:17.42+12:19:42.8	−17.96	0.23	−19.29	0.11	−19.96	0.10	−20.31	0.17	−20.61	0.19	10.1	1
NGVS J12:30:17.45+12:14:28.3	−11.48	0.14	−12.68	0.06	−13.12	0.05	−13.32	0.17	−12.54	0.19	7.1	0
NGVS J12:30:18.00+12:02:30.5	−10.80	0.29	−11.91	0.10	−12.46	0.11	−12.66	0.14	−12.27	0.72	6.8	0
NGVS J12:30:18.21+12:34:17.3	−10.54	0.24	−11.55	0.08	−11.98	0.09	−12.39	0.16	−12.20	0.19	6.7	0
NGVS J12:30:19.94+11:43:21.0	−10.06	0.91	−10.57	0.28	−10.96	0.29	−11.55	0.17	−11.33	0.76	6.3	0
NGVS J12:30:20.43+12:49:00.4	−9.62	0.23	−10.42	0.67	−10.99	0.34	−11.00	0.57	−11.49	0.69	6.1	0
NGVS J12:30:21.67+11:40:16.7	−7.80	0.23	−8.28	0.38	−8.38	0.46	−9.58	0.95	−7.21	1.32	5.4	0
NGVS J12:30:23.85+12:26:07.2	−8.96	0.23	−11.44	0.26	−12.05	0.29	−12.13	0.48	−10.59	0.19	6.6	0
NGVS J12:30:24.05+13:18:45.0	−7.45	0.69	−9.02	0.44	−9.58	0.56	−9.71	0.65	−9.64	1.45	5.5	0
NGVS J12:30:24.48+13:19:55.8	−12.19	0.12	−13.04	0.05	−13.59	0.05	−13.87	0.06	−13.95	0.10	7.3	0
NGVS J12:30:24.56+12:47:34.4	−10.95	0.23	−11.95	0.10	−12.51	0.09	−12.71	0.13	−12.83	0.21	6.8	0
NGVS J12:30:26.92+12:56:08.2	−9.53	0.36	−10.62	0.31	−11.14	0.24	−11.75	0.27	−12.11	1.40	6.4	0
NGVS J12:30:27.53+12:52:25.6	−8.40	0.23	−9.00	0.42	−9.45	0.41	−9.72	0.47	−9.15	0.39	5.5	0
NGVS J12:30:28.29+12:58:57.1	−10.58	0.22	−11.42	0.10	−11.84	0.09	−12.15	0.14	−12.36	0.27	6.6	0
NGVS J12:30:30.48+13:05:39.3	−10.00	0.16	−11.02	0.06	−11.46	0.06	−11.66	0.10	−11.74	0.31	6.4	0
NGVS J12:30:31.97+12:29:24.6	−15.79	0.23	−17.33	0.11	−18.03	0.10	−18.41	0.17	−18.73	0.19	9.3	0
NGVS J12:30:32.18+12:51:51.2	−9.66	0.23	−10.81	0.19	−11.31	0.09	−11.36	0.25	−11.50	1.30	6.2	1
NGVS J12:30:33.32+12:54:02.3	−12.33	0.06	−13.34	0.03	−13.85	0.03	−14.17	0.04	−14.23	0.06	7.4	0
NGVS J12:30:34.65+12:27:29.2	−11.93	0.11	−12.88	0.04	−13.48	0.05	−13.97	0.08	−13.04	0.10	7.3	0
NGVS J12:30:35.12+13:11:20.2	−9.21	0.39	−10.44	0.13	−11.16	0.15	−11.30	0.19	−11.18	0.45	6.2	0
NGVS J12:30:37.24+12:46:09.2	−10.92	0.23	−12.13	0.11	−12.73	0.10	−12.82	0.17	−13.16	0.19	6.9	0
NGVS J12:30:37.35+13:00:33.3	−9.96	0.32	−10.93	0.10	−11.36	0.08	−11.45	0.14	−11.91	0.20	6.3	0
NGVS J12:30:40.41+12:37:17.8	−9.06	0.23	−10.05	0.11	−10.44	0.10	−10.64	0.35	−10.63	0.19	5.9	1
NGVS J12:30:42.65+12:47:26.1	−8.83	1.01	−10.02	0.42	−10.60	0.10	−10.39	0.78	−10.15	0.19	5.8	0
NGVS J12:30:46.32+12:05:56.7	−13.00	0.04	−13.52	0.03	−13.80	0.03	−13.83	0.04	−13.97	0.04	7.3	0
NGVS J12:30:46.32+12:36:49.5	−8.25	0.73	−9.25	0.47	−9.76	0.10	−9.87	0.53	−10.35	0.19	5.6	0
NGVS J12:30:46.88+13:12:50.4	−10.79	0.15	−11.53	0.05	−12.04	0.04	−12.29	0.06	−12.46	0.18	6.6	0
NGVS J12:30:47.20+11:32:15.4	−11.16	0.12	−12.26	0.06	−12.79	0.05	−13.01	0.07	−13.17	0.10	6.9	0

Table 4
(Continued)

ID	M_u	Δu	M_g	Δg	M_r	Δr	M_i	Δi	M_z	Δz	log $(M_*/M_\odot)$	Nucleation
NGVS J12:30:48.58+12:02:42.7	−13.67	0.04	−14.15	0.02	−14.20	0.02	−13.88	0.05	−14.09	0.06	7.3	0
NGVS J12:30:49.03+13:13:25.8	−13.39	0.03	−14.34	0.02	−14.83	0.01	−15.06	0.02	−15.15	0.03	7.8	0
NGVS J12:30:49.42+12:23:28.0	−21.51	0.23	−22.55	0.10	−23.09	0.10	−23.40	0.10	−23.66	0.10	11.4	0
NGVS J12:30:50.59+12:44:11.7	−12.29	0.04	−13.32	0.02	−13.78	0.02	−14.00	0.04	−14.16	0.04	7.4	1
NGVS J12:30:53.26+11:39:15.5	−8.36	1.01	−8.56	0.21	−9.54	0.50	−9.89	0.86	−9.04	0.92	5.6	0
NGVS J12:30:55.66+13:20:53.8	−12.43	0.07	−13.30	0.02	−13.73	0.02	−13.94	0.03	−13.99	0.06	7.3	0
NGVS J12:30:57.37+13:13:51.7	−9.05	0.53	−10.03	0.21	−10.48	0.16	−10.71	0.28	−11.13	0.19	6.0	0
NGVS J12:30:57.77+12:16:15.5	−16.88	0.04	−18.22	0.02	−18.94	0.02	−19.32	0.03	−19.65	0.02	9.7	1
NGVS J12:30:58.81+11:42:30.8	−12.76	0.09	−13.77	0.05	−14.36	0.05	−14.48	0.17	−14.60	0.09	7.6	0
NGVS J12:31:03.19+12:21:10.5	−10.32	0.33	−11.14	0.19	−11.67	0.21	−11.87	0.29	−11.88	0.34	6.5	0
NGVS J12:31:03.28+12:04:40.6	−10.47	0.17	−11.48	0.06	−12.14	0.07	−12.13	0.09	−12.31	0.15	6.6	0
NGVS J12:31:03.98+11:50:10.2	−12.70	0.10	−13.59	0.04	−14.24	0.05	−14.42	0.05	−14.50	0.10	7.5	0
NGVS J12:31:05.15+12:29:38.3	−9.64	0.23	−10.64	0.11	−10.98	0.10	−11.27	0.17	−11.46	0.19	6.2	0
NGVS J12:31:05.67+12:49:38.9	−7.56	1.25	−9.00	0.73	−9.20	0.55	−9.37	0.96	−9.24	1.34	5.3	0
NGVS J12:31:09.67+13:21:15.5	−7.58	0.93	−8.56	0.53	−9.05	0.34	−9.64	0.59	−9.87	0.82	5.4	0
NGVS J12:31:10.42+13:05:50.5	−12.37	0.09	−13.34	0.04	−13.86	0.03	−14.07	0.05	−14.19	0.06	7.4	1
NGVS J12:31:11.64+13:06:51.7	−11.77	0.07	−12.89	0.03	−13.36	0.03	−13.60	0.04	−13.67	0.07	7.2	0
NGVS J12:31:11.78+12:03:48.5	−7.04	1.12	−8.41	0.34	−9.24	0.55	−9.24	0.79	−10.32	0.90	5.3	0
NGVS J12:31:12.69+13:07:27.4	−12.14	0.05	−13.13	0.03	−13.59	0.03	−13.84	0.04	−13.89	0.05	7.3	0
NGVS J12:31:15.73+12:19:54.4	−14.61	0.02	−15.89	0.11	−16.50	0.10	−16.90	0.01	−17.15	0.01	8.6	1
NGVS J12:31:16.55+12:03:58.2	−8.34	0.85	−8.74	0.29	−9.37	0.38	−9.18	0.59	−9.08	0.31	5.2	0
NGVS J12:31:18.87+13:19:54.7	−11.56	0.07	−12.61	0.04	−13.10	0.02	−13.34	0.04	−13.38	0.05	7.1	1
NGVS J12:31:19.41+12:40:13.2	−6.19	0.23	−8.30	0.66	−8.88	0.81	−8.82	0.41	−8.73	1.20	5.1	0
NGVS J12:31:19.43+12:44:16.9	−13.89	0.01	−14.92	0.11	−15.42	0.10	−15.65	0.17	−15.76	0.01	8.1	1
NGVS J12:31:19.57+12:36:41.5	−13.13	0.03	−14.22	0.01	−14.72	0.01	−15.04	0.02	−15.13	0.03	7.8	0
NGVS J12:31:20.29+11:31:49.4	−10.12	0.26	−10.88	0.06	−11.17	0.07	−11.45	0.20	−11.59	0.17	6.3	0
NGVS J12:31:24.42+13:20:56.7	−9.60	0.37	−10.86	0.21	−11.26	0.17	−11.54	0.29	−11.78	0.54	6.3	0
NGVS J12:31:28.07+12:51:18.3	−10.93	0.17	−11.59	0.12	−11.89	0.13	−12.12	0.15	−12.37	0.30	6.6	0
NGVS J12:31:28.82+12:06:50.3	−9.11	0.23	−12.53	0.31	−13.67	0.46	−12.73	0.17	−13.84	0.19	6.8	0
NGVS J12:31:30.70+12:59:00.2	−6.90	0.23	−8.38	0.70	−8.52	0.31	−9.43	1.36	−8.96	0.23	5.3	0
NGVS J12:31:30.92+12:56:11.2	−8.35	0.93	−8.83	0.31	−9.28	0.29	−9.47	0.67	−9.83	0.52	5.4	0
NGVS J12:31:31.68+11:36:11.1	−13.08	0.12	−14.22	0.06	−14.75	0.07	−15.13	0.08	−15.31	0.08	7.9	1
NGVS J12:31:32.54+11:37:29.1	−17.11	0.23	−18.37	0.11	−18.97	0.10	−19.30	0.17	−19.53	0.19	9.7	1
NGVS J12:31:33.35+12:03:49.7	−13.35	0.04	−14.46	0.01	−14.90	0.02	−15.19	0.03	−15.32	0.03	7.9	1
NGVS J12:31:33.92+12:04:03.2	−11.00	0.21	−12.25	0.15	−12.72	0.09	−13.02	0.16	−12.53	0.17	7.0	1
NGVS J12:31:34.12+12:54:17.6	−6.65	1.38	−9.11	0.80	−9.51	0.88	−10.13	0.51	−7.41	0.19	5.7	0
NGVS J12:31:35.09+11:54:46.9	−8.66	0.39	−9.38	0.61	−9.93	0.57	−10.38	0.98	−10.99	0.08	5.8	0
NGVS J12:31:35.38+12:10:07.4	−11.22	0.50	−12.44	0.11	−13.32	0.11	−12.53	0.17	−13.43	0.29	6.7	0
NGVS J12:31:36.13+12:20:12.2	−6.65	0.24	−8.03	0.49	−8.36	0.17	−8.47	0.17	−6.51	0.19	4.9	0
NGVS J12:31:36.42+13:05:19.7	−11.07	0.20	−12.35	0.11	−12.77	0.10	−13.07	0.17	−13.16	0.19	7.0	0
NGVS J12:31:37.22+12:46:30.8	−9.40	0.79	−9.76	0.21	−10.16	0.19	−10.38	0.31	−10.42	0.19	5.8	0
NGVS J12:31:38.75+11:49:44.7	−8.92	0.07	−9.95	0.29	−10.29	0.25	−10.62	0.54	−11.27	0.35	5.9	1
NGVS J12:31:41.52+11:48:04.6	−7.63	0.23	−7.74	0.11	−8.88	0.43	−9.29	0.17	−8.82	0.19	5.3	0
NGVS J12:31:43.84+11:51:51.3	−7.85	0.56	−8.91	0.29	−9.49	0.45	−9.58	0.58	−10.47	0.19	5.4	0
NGVS J12:31:44.03+12:36:44.6	−11.32	0.11	−12.48	0.04	−12.98	0.04	−13.23	0.06	−13.50	0.10	7.0	0
NGVS J12:31:47.45+12:58:14.4	−8.30	0.23	−9.07	0.62	−9.44	0.24	−9.58	0.77	−10.02	0.93	5.4	0
NGVS J12:31:47.86+12:18:21.5	−8.12	1.27	−9.38	0.36	−10.08	0.36	−10.09	0.49	−9.93	0.90	5.7	0
NGVS J12:31:48.01+12:21:33.1	−9.50	1.42	−11.34	0.55	−11.63	0.07	−12.10	0.48	−11.99	0.74	6.6	0
NGVS J12:31:51.33+12:39:25.2	−15.43	0.01	−16.59	0.11	−17.19	0.10	−17.54	0.17	−17.61	0.01	8.9	1
NGVS J12:31:52.01+12:28:54.5	−14.24	0.01	−15.36	0.11	−15.91	0.10	−16.17	0.01	−16.34	0.01	8.3	1
NGVS J12:31:52.90+12:15:59.1	−12.10	0.23	−13.29	0.03	−13.91	0.04	−14.21	0.03	−14.41	0.02	7.5	1
NGVS J12:31:53.09+13:15:44.1	−8.00	1.00	−9.97	0.65	−10.27	0.57	−10.23	0.79	−10.16	0.80	5.7	1
NGVS J12:31:55.11+12:56:43.0	−7.54	0.96	−7.96	0.44	−8.69	0.10	−8.97	0.17	−8.71	0.19	5.1	0
NGVS J12:31:55.93+12:10:27.0	−15.30	0.02	−16.56	0.11	−17.14	0.10	−17.48	0.17	−17.72	0.01	8.9	1
NGVS J12:31:56.40+11:58:21.6	−13.02	0.07	−14.03	0.03	−14.69	0.02	−14.95	0.03	−15.11	0.04	7.8	1
NGVS J12:32:00.19+13:04:55.4	−13.19	0.07	−14.20	0.02	−14.61	0.03	−14.92	0.03	−14.63	0.19	7.8	0
NGVS J12:32:00.75+12:37:13.2	−13.35	0.03	−14.53	0.01	−15.04	0.01	−15.33	0.01	−15.47	0.02	7.9	1
NGVS J12:32:01.12+13:04:31.5	−8.99	0.66	−10.15	0.36	−10.70	0.35	−10.97	0.40	−11.65	0.75	6.1	0
NGVS J12:32:01.88+13:24:02.0	−6.74	0.23	−7.99	0.48	−8.57	0.45	−8.90	0.59	−9.75	1.07	5.1	0
NGVS J12:32:02.74+11:53:24.3	−15.10	0.01	−16.30	0.11	−16.89	0.10	−17.22	0.17	−17.37	0.19	8.8	1
NGVS J12:32:03.77+13:04:25.1	−8.71	1.28	−9.84	0.31	−10.37	0.21	−10.34	0.32	−9.67	0.19	5.8	0
NGVS J12:32:03.79+12:34:010.0	−8.22	0.32	−8.95	0.33	−9.35	0.14	−9.56	0.47	−10.37	0.28	5.4	0
NGVS J12:32:04.80+12:23:42.0	−9.71	0.23	−10.75	0.08	−11.22	0.08	−11.48	0.13	−11.78	0.27	6.3	0
NGVS J12:32:05.63+11:49:03.6	−14.87	0.02	−15.72	0.01	−16.08	0.02	−16.29	0.02	−16.41	0.02	8.4	1
NGVS J12:32:07.65+12:26:02.9	−12.12	0.12	−13.24	0.05	−13.74	0.05	−14.06	0.06	−14.25	0.11	7.4	1

Table 4
(Continued)

ID	M_u	Δu	M_g	Δg	M_r	Δr	M_i	Δi	M_z	Δz	log $(M_*/M_\odot)$	Nucleation
NGVS J12:32:09.31+12:50:20.2	−13.16	0.03	−14.22	0.01	−14.71	0.01	−14.98	0.02	−15.05	0.02	7.8	1
NGVS J12:32:10.28+12:33:02.2	−10.74	0.57	−11.11	0.26	−11.70	0.17	−11.98	0.29	−12.60	0.41	6.5	0
NGVS J12:32:10.50+13:25:09.7	−16.83	0.01	−17.92	0.11	−18.50	0.10	−18.76	0.17	−19.01	0.19	9.5	1
NGVS J12:32:11.36+12:30:24.9	−13.00	0.06	−14.10	0.02	−14.59	0.02	−14.89	0.02	−15.14	0.05	7.8	1
NGVS J12:32:12.24+12:03:41.5	−13.76	0.02	−14.90	0.11	−15.42	0.10	−15.75	0.01	−15.84	0.01	8.1	1
NGVS J12:32:14.52+11:47:26.5	−10.91	0.18	−11.23	0.08	−11.65	0.08	−11.90	0.12	−11.81	0.19	6.5	0
NGVS J12:32:22.52+12:19:32.1	−11.18	0.13	−11.89	1.10	−12.18	0.41	−12.62	0.10	−12.66	0.19	6.8	0
NGVS J12:32:23.58+11:53:36.1	−14.62	0.02	−15.68	0.01	−16.15	0.01	−16.46	0.02	−16.59	0.02	8.4	0
NGVS J12:32:24.04+11:45:31.5	−9.88	0.42	−10.73	0.10	−11.28	0.12	−11.33	0.16	−11.49	0.24	6.2	0
NGVS J12:32:25.47+12:08:52.9	−9.72	0.23	−10.63	0.18	−10.93	0.19	−11.48	0.28	−11.64	0.34	6.3	0
NGVS J12:32:25.50+13:05:29.3	−8.23	0.23	−9.89	0.11	−10.27	0.21	−10.40	0.39	−10.59	0.19	5.8	0
NGVS J12:32:26.21+12:43:48.2	−8.28	0.65	−9.32	0.33	−9.86	0.28	−9.72	0.53	−10.52	1.03	5.5	0
NGVS J12:32:26.22+11:45:01.7	−7.87	0.77	−8.87	0.60	−9.83	0.69	−9.85	0.85	−9.26	0.43	5.6	0
NGVS J12:32:26.53+11:37:20.7	−5.60	0.23	−10.06	0.88	−10.21	0.34	−10.29	0.53	−10.91	0.19	5.8	0
NGVS J12:32:29.96+11:50:01.3	−10.21	0.58	−11.00	0.20	−11.56	0.18	−11.84	0.33	−12.62	0.96	6.5	0
NGVS J12:32:32.48+11:42:00.3	−8.22	0.30	−9.07	0.24	−9.48	0.24	−9.98	0.35	−10.35	0.65	5.6	0
NGVS J12:32:33.45+12:47:21.6	−9.40	0.20	−10.52	0.24	−10.99	0.21	−11.12	0.24	−11.30	0.20	6.1	0
NGVS J12:32:34.71+12:38:21.1	−12.34	0.16	−13.66	0.06	−14.11	0.06	−14.25	0.08	−14.47	0.15	7.5	0
NGVS J12:32:38.96+12:17:36.7	−8.75	0.38	−9.67	0.11	−10.14	0.14	−10.39	0.22	−10.42	0.38	5.8	0
NGVS J12:32:39.13+13:19:47.5	−12.42	0.10	−13.46	0.03	−13.97	0.03	−14.23	0.04	−14.38	0.07	7.5	0
NGVS J12:32:39.99+11:53:43.7	−7.92	0.23	−9.00	1.24	−9.40	0.64	−9.18	1.07	−10.14	0.19	5.2	1
NGVS J12:32:40.80+12:46:15.9	−16.19	0.01	−17.40	0.11	−17.92	0.10	−18.21	0.17	−18.32	0.01	9.2	0
NGVS J12:32:50.56+12:08:20.8	−9.67	0.15	−10.59	0.10	−11.17	0.09	−11.30	0.21	−11.52	0.08	6.2	1
NGVS J12:32:54.11+12:48:27.2	−11.84	0.08	−12.80	0.04	−13.34	0.04	−13.61	0.04	−13.74	0.06	7.2	0
NGVS J12:32:54.78+11:57:26.2	−8.01	1.08	−9.22	0.40	−9.61	0.60	−10.02	0.87	−9.98	1.19	5.6	0
NGVS J12:32:55.32+12:20:58.0	−6.48	0.23	−8.41	0.55	−8.89	0.35	−9.04	0.17	−7.63	1.27	5.2	0
NGVS J12:32:55.32+12:38:06.9	−10.90	0.14	−11.91	0.05	−12.41	0.05	−12.70	0.06	−12.76	0.09	6.8	0
NGVS J12:32:55.36+12:45:33.2	−9.06	0.59	−10.39	0.20	−10.87	0.17	−10.97	0.27	−11.30	0.19	6.1	0
NGVS J12:32:55.68+13:13:56.9	−8.51	0.51	−9.53	0.29	−9.78	0.21	−10.26	0.32	−10.35	0.43	5.7	0
NGVS J12:33:00.82+11:54:52.6	−5.81	0.23	−8.18	0.55	−8.79	0.58	−9.05	0.72	−9.46	0.84	5.2	0
NGVS J12:33:03.96+12:53:15.4	−8.18	0.87	−9.48	0.35	−9.96	0.32	−9.93	0.17	−10.18	0.19	5.6	0
NGVS J12:33:05.74+13:09:39.7	−11.30	0.09	−12.30	0.04	−12.81	0.04	−12.99	0.05	−13.29	0.14	6.9	0
NGVS J12:33:05.99+11:32:01.3	−9.64	0.17	−11.01	0.04	−11.62	0.05	−11.87	0.05	−12.07	0.11	6.5	1
NGVS J12:33:06.02+11:55:22.9	−7.33	0.23	−8.14	0.47	−8.55	0.50	−8.60	0.17	−8.03	0.19	5.0	0
NGVS J12:33:06.41+13:18:11.1	−11.94	0.17	−12.87	0.08	−13.45	0.07	−13.66	0.13	−13.94	0.12	7.2	1
NGVS J12:33:07.21+13:08:24.6	−6.98	0.06	−7.86	0.55	−8.40	0.60	−8.18	1.04	−8.59	0.11	4.8	0
NGVS J12:33:07.52+12:12:13.4	−10.21	0.23	−11.28	0.16	−11.75	0.13	−12.48	0.23	−12.66	0.35	6.7	1
NGVS J12:33:07.97+12:30:08.9	−7.82	0.23	−9.60	0.92	−10.13	0.84	−10.22	0.48	−10.91	0.47	5.7	0
NGVS J12:33:08.68+12:10:57.8	−9.48	0.20	−10.46	0.11	−10.92	0.10	−11.38	0.12	−11.22	0.19	6.3	0
NGVS J12:33:09.53+12:16:57.3	−11.95	0.09	−13.14	0.04	−13.66	0.04	−14.04	0.06	−14.02	0.11	7.4	0
NGVS J12:33:10.17+12:05:09.9	−10.23	0.21	−11.04	0.11	−11.51	0.07	−11.73	0.15	−11.80	0.25	6.4	1
NGVS J12:33:11.87+12:42:55.7	−7.19	0.23	−8.10	0.60	−8.90	0.60	−9.06	1.29	−9.06	1.43	5.2	0
NGVS J12:33:14.01+12:51:28.2	−14.94	0.23	−16.23	0.11	−16.83	0.10	−17.13	0.17	−17.24	0.19	8.7	1
NGVS J12:33:14.02+11:46:53.6	−8.68	0.58	−9.24	0.44	−9.79	0.38	−9.84	0.20	−10.12	0.56	5.5	0
NGVS J12:33:15.73+11:52:07.0	−9.67	0.48	−11.00	0.25	−11.49	0.18	−11.80	0.25	−12.39	1.08	6.4	0
NGVS J12:33:15.83+13:13:10.3	−7.88	0.79	−9.33	1.08	−9.87	0.32	−9.80	1.08	−9.29	0.37	5.5	0
NGVS J12:33:16.88+12:16:56.2	−10.55	0.36	−11.58	0.09	−12.17	0.09	−12.28	0.12	−12.44	0.17	6.6	0
NGVS J12:33:16.91+12:34:54.5	−11.40	0.10	−12.31	0.03	−12.80	0.04	−13.05	0.07	−13.30	0.08	7.0	0
NGVS J12:33:17.19+11:37:36.4	−7.80	0.23	−9.45	0.24	−9.91	0.32	−10.11	0.50	−10.68	0.78	5.7	0
NGVS J12:33:17.38+12:34:54.5	−8.07	0.60	−9.53	0.19	−10.18	0.20	−10.49	0.30	−9.04	0.19	5.8	0
NGVS J12:33:19.79+12:51:12.5	−15.40	0.23	−16.26	0.11	−16.59	0.10	−16.81	0.17	−16.90	0.19	8.6	0
NGVS J12:33:22.53+11:38:29.4	−10.77	0.12	−11.92	0.05	−12.47	0.05	−12.71	0.07	−12.75	0.08	6.8	0
NGVS J12:33:24.73+12:24:11.3	−9.17	0.58	−10.10	0.17	−10.69	0.17	−10.90	0.32	−10.87	0.52	6.0	0
NGVS J12:33:25.21+13:24:58.5	−11.49	0.24	−12.83	0.07	−13.18	0.07	−13.57	0.10	−13.71	0.20	7.2	0
NGVS J12:33:29.44+13:17:22.8	−8.06	0.36	−8.36	0.79	−8.80	0.60	−9.34	0.32	−9.23	0.72	5.3	0
NGVS J12:33:30.72+13:00:21.5	−7.95	0.64	−9.00	0.60	−9.55	0.44	−9.79	0.60	−9.97	1.36	5.5	0
NGVS J12:33:32.45+12:15:45.0	−7.25	1.11	−8.80	0.11	−9.66	0.29	−9.52	0.17	−9.63	1.25	5.4	0
NGVS J12:33:36.86+13:21:45.4	−7.65	1.30	−8.18	0.32	−8.90	0.28	−9.11	0.66	−9.26	1.15	5.2	0
NGVS J12:33:40.31+12:44:13.6	−11.95	0.08	−12.91	0.05	−13.42	0.03	−13.68	0.05	−13.88	0.05	7.2	1
NGVS J12:33:40.81+12:34:16.4	−12.47	0.09	−13.55	0.03	−13.99	0.02	−14.26	0.03	−14.52	0.05	7.5	1
NGVS J12:33:40.91+12:22:56.7	−11.50	0.10	−12.50	0.04	−13.02	0.04	−13.25	0.06	−13.43	0.08	7.0	0
NGVS J12:33:44.70+11:40:57.1	−9.72	0.39	−10.76	0.15	−11.59	0.24	−11.54	0.16	−11.84	0.17	6.3	1
NGVS J12:33:47.06+11:46:53.8	−12.21	0.39	−13.22	0.07	−13.88	0.09	−14.04	0.12	−14.04	0.23	7.4	1
NGVS J12:33:48.67+12:46:48.1	−12.60	0.05	−13.72	0.02	−14.26	0.02	−14.57	0.03	−14.68	0.03	7.6	1
NGVS J12:33:49.57+13:02:20.3	−10.91	0.23	−11.33	0.20	−11.85	0.14	−12.40	0.30	−11.76	0.19	6.7	1

Table 4
(Continued)

ID	M_u	Δu	M_g	Δg	M_r	Δr	M_i	Δi	M_z	Δz	$\log(M_*/M_\odot)$	Nucleation
NGVS J12:33:51.12+12:57:30.3	−11.16	0.13	−12.06	0.07	−12.54	0.07	−12.78	0.10	−12.81	0.14	6.9	1
NGVS J12:33:51.62+13:19:20.9	−15.62	0.23	−16.84	0.11	−17.44	0.10	−17.77	0.17	−17.95	0.19	9.0	0
NGVS J12:33:52.35+13:14:54.6	−8.32	1.41	−8.75	1.04	−9.13	0.61	−9.64	0.49	−10.20	1.31	5.5	0
NGVS J12:33:52.50+12:07:02.5	−9.90	0.69	−10.79	0.15	−11.17	0.15	−11.52	0.23	−11.45	0.61	6.3	0
NGVS J12:33:58.18+13:13:14.9	−8.97	0.23	−10.20	0.34	−10.60	0.23	−10.71	0.47	−9.81	0.19	6.0	0
NGVS J12:34:01.39+12:43:11.2	−10.96	0.29	−11.98	0.09	−12.49	0.07	−12.77	0.12	−12.92	0.22	6.8	1
NGVS J12:34:06.56+11:50:12.1	−12.26	0.12	−13.20	0.04	−13.73	0.04	−14.02	0.06	−14.16	0.07	7.4	1
NGVS J12:34:06.74+12:44:29.7	−14.53	0.03	−15.62	0.11	−16.18	0.10	−16.49	0.01	−16.69	0.02	8.5	1
NGVS J12:34:07.61+12:38:52.6	−8.81	0.42	−9.76	0.16	−10.22	0.13	−10.44	0.23	−10.31	0.60	5.8	0
NGVS J12:34:07.83+11:45:48.1	−8.40	0.23	−10.49	0.11	−11.14	0.10	−11.13	0.17	−11.12	0.19	6.1	1
NGVS J12:34:08.81+11:34:30.7	−6.50	0.23	−8.03	0.79	−8.79	0.68	−8.63	0.17	−9.31	0.63	5.0	0
NGVS J12:34:08.98+12:44:24.8	−11.10	0.15	−12.07	0.06	−12.88	0.08	−13.19	0.10	−13.48	0.15	7.0	1

Table 5
Photometry of NGVS Nuclei

ID	M_u	Δu	M_g	Δg	M_r	Δr	M_i	Δi	M_z	Δz	$\log(M_*/M_\odot)$
NGVS J12:26:22.61+12:47:11.0	−2.75	0.62	−8.28	0.04	−8.89	0.01	−7.73	0.09	−5.57	0.48	5.0
NGVS J12:26:23.64+13:22:24.7	−6.27	0.02	−7.36	0.01	−7.89	0.02	−8.12	0.02	−7.97	0.06	5.2
NGVS J12:26:28.06+12:55:14.2	−7.53	0.03	−8.58	0.03	−9.20	0.03	−9.26	0.04	−9.69	0.02	5.6
NGVS J12:26:33.21+12:44:34.7	−8.78	0.05	−10.46	0.26	−11.22	0.21	−11.45	0.23	−11.90	0.04	6.5
NGVS J12:26:36.32+12:48:10.0	−8.71	0.04	−9.74	0.03	−10.21	0.03	−10.48	0.06	−10.53	0.03	6.1
NGVS J12:26:38.09+11:53:30.7	−6.85	0.68	−7.47	0.13	−8.03	0.62	−8.29	0.69	−8.42	0.00	5.2
NGVS J12:26:38.25+13:04:44.2	−8.91	0.28	−9.99	0.20	−10.49	0.20	−10.70	0.24	−10.82	0.94	6.2
NGVS J12:26:39.81+12:30:48.8	−8.82	0.00	−9.92	0.01	−10.45	0.01	−10.79	0.04	−10.84	0.03	6.2
NGVS J12:26:43.31+12:17:44.0	−9.16	0.03	−10.16	0.11	−10.68	0.06	−10.90	0.08	−11.07	0.00	6.3
NGVS J12:26:47.06+12:27:14.3	−9.90	0.09	−11.08	0.06	−11.65	0.03	−11.98	0.05	−12.16	0.07	6.7
NGVS J12:26:51.99+12:39:08.2	−6.86	0.77	−7.59	0.02	−8.07	0.77	−8.21	0.72	−8.25	1.08	5.2
NGVS J12:26:54.36+11:39:50.2	−9.99	0.03	−10.41	0.04	−10.69	0.01	−10.79	0.01	−10.86	0.08	6.2
NGVS J12:27:03.08+12:33:38.8	−9.78	0.19	−10.80	0.11	−11.29	0.16	−11.59	0.16	−11.68	0.03	6.6
NGVS J12:27:08.42+13:20:08.7	−8.46	0.43	−9.39	0.03	−9.88	0.14	−10.13	0.15	−10.32	0.02	6.0
NGVS J12:27:11.24+12:02:17.4	−7.24	0.19	−7.99	0.01	−8.76	0.01	−8.88	0.01	−9.21	0.01	5.5
NGVS J12:27:13.34+12:44:05.2	−11.33	0.02	−13.40	0.01	22.47	0.01	−13.41	0.02	−15.11	0.01	7.3
NGVS J12:27:16.78+12:32:07.8	−6.32	0.00	−7.28	0.01	−7.92	0.07	−8.14	0.01	−8.20	0.55	5.2
NGVS J12:27:22.17+12:04:07.4	−7.97	0.00	−8.94	0.01	−9.50	0.06	−9.76	0.07	−9.86	0.08	5.8
NGVS J12:27:29.78+12:15:07.2	−6.88	0.02	−7.93	0.34	−8.32	0.29	−8.56	0.29	−8.66	0.00	5.3
NGVS J12:27:32.01+11:36:54.7	−7.40	0.01	−8.36	0.01	−8.95	0.01	−9.16	0.01	−9.33	0.00	5.6
NGVS J12:27:33.18+11:31:55.7	−7.96	0.00	−8.55	0.43	−8.03	1.12	−7.96	0.01	−131.09	0.00	5.1
NGVS J12:27:39.24+12:52:47.6	−8.34	0.22	−9.33	0.16	−9.78	0.17	−10.03	0.21	−10.16	0.23	5.9
NGVS J12:27:41.24+12:18:57.2	−9.69	0.00	−11.08	0.01	−11.78	0.01	−12.11	0.01	−12.31	0.00	6.8
NGVS J12:27:44.52+12:59:01.3	−8.89	0.61	−9.89	0.06	−10.36	0.07	−10.63	0.14	−10.68	0.17	6.2
NGVS J12:27:53.57+12:17:35.8	−15.59	0.00	−131.09	0.01	−15.00	0.01	−17.58	0.01	−13.90	0.05	9.0
NGVS J12:28:00.44+11:56:59.6	−7.95	0.00	−8.89	0.01	−9.43	0.06	−9.67	0.01	−9.57	0.05	5.8
NGVS J12:28:03.74+12:46:41.2	−8.11	0.13	−9.01	0.04	−9.49	0.14	−9.64	0.13	−9.80	0.17	5.8
NGVS J12:28:06.53+12:53:53.3	−8.70	0.00	−9.70	0.01	−10.18	0.01	−10.45	0.01	−10.49	0.00	6.1
NGVS J12:28:06.77+12:58:43.2	−8.36	0.36	−9.29	0.30	−9.75	0.35	−10.00	0.39	−10.07	0.15	5.9
NGVS J12:28:08.61+12:05:35.8	−9.75	0.00	−11.01	0.01	−11.67	0.48	−11.95	0.01	−12.18	0.22	6.7
NGVS J12:28:10.28+12:48:32.2	−7.75	0.03	−8.61	0.05	−9.11	0.01	−9.38	0.42	−9.12	0.12	5.7
NGVS J12:28:12.24+11:58:13.3	−5.93	0.06	−6.67	0.01	−7.26	0.54	−7.28	0.01	−7.99	1.47	4.8
NGVS J12:28:14.87+11:47:23.6	−9.48	0.00	−11.02	0.01	−131.09	0.01	−11.89	0.01	−12.44	0.00	6.7
NGVS J12:28:18.74+11:42:00.9	−9.88	0.06	−10.93	0.04	−11.44	0.04	−11.70	0.05	−11.80	0.07	6.6
NGVS J12:28:21.66+12:08:04.0	−6.69	0.01	−7.49	0.02	−7.95	0.24	−8.16	0.03	−8.51	0.47	5.2
NGVS J12:28:23.64+13:11:44.7	−8.68	0.04	−9.67	0.01	−10.04	0.03	−10.33	0.42	−10.29	0.01	6.1
NGVS J12:28:26.26+12:20:45.2	−7.93	0.00	−8.88	0.01	−9.34	0.01	−9.57	0.20	−9.65	0.40	5.8
NGVS J12:28:28.06+12:49:25.3	−8.84	0.00	−9.90	0.01	−10.43	0.01	−10.73	0.01	−10.80	0.00	6.2
NGVS J12:28:41.71+12:54:57.2	−9.47	0.00	−10.62	0.01	−11.07	0.01	−11.43	0.01	−11.57	0.00	6.5
NGVS J12:28:42.66+12:32:59.4	−8.87	0.29	−9.93	0.14	−10.37	0.18	−10.55	0.17	−10.75	0.02	6.1
NGVS J12:28:46.92+12:38:31.5	−7.16	0.76	−8.00	0.04	−8.41	0.05	−8.64	0.05	−8.83	0.68	5.4
NGVS J12:28:57.68+11:57:20.2	−5.58	0.70	−6.81	0.01	−7.35	0.11	−7.30	0.07	28.03	0.00	4.8
NGVS J12:28:58.14+12:39:42.2	−11.41	0.09	−13.02	0.03	−13.33	0.09	−13.92	0.01	−14.13	0.12	7.5
NGVS J12:28:59.15+12:02:30.4	−6.77	0.30	−7.66	0.02	−8.15	0.01	−8.37	0.52	−8.51	0.67	5.3
NGVS J12:28:59.50+11:55:23.4	−6.91	0.97	−8.02	0.36	−8.48	0.49	−8.65	0.01	−8.76	0.00	5.4
NGVS J12:28:59.82+12:38:54.2	−5.63	0.00	−7.20	0.01	−7.61	0.01	−7.10	0.07	−7.44	0.10	4.8

Table 5
(Continued)

ID	M_u	Δu	M_g	Δg	M_r	Δr	M_i	Δi	M_z	Δz	$\log (M_*/M_\odot)$
NGVS J12:29:03.01+13:11:01.7	−15.17	0.00	−17.61	0.01	−18.12	0.01	−18.62	0.01	−18.95	0.00	9.4
NGVS J12:29:05.13+12:09:13.6	−8.10	0.11	−9.13	0.22	−9.61	0.17	−9.84	0.30	−10.05	0.00	5.9
NGVS J12:29:12.31+11:31:11.9	−7.59	0.29	−8.46	0.01	−8.92	0.01	−9.15	0.05	−9.46	0.00	5.6
NGVS J12:29:14.85+12:58:41.7	−6.81	0.01	−7.71	0.01	−8.32	0.01	−8.44	0.01	−8.19	0.03	5.3
NGVS J12:29:23.52+12:27:02.9	−9.23	0.00	−10.36	0.03	−10.84	0.03	−11.15	0.04	−11.26	0.03	6.4
NGVS J12:29:28.67+12:29:46.3	−7.77	0.77	−9.52	0.04	−9.98	0.03	−10.23	0.14	−8.65	0.12	6.0
NGVS J12:29:39.06+11:38:00.3	−8.46	0.24	−9.36	0.07	−10.00	0.12	−10.25	0.13	−10.43	0.18	6.0
NGVS J12:29:39.24+12:32:53.7	−9.64	0.05	−10.77	0.03	−11.24	0.04	−11.52	0.04	−11.63	0.09	6.5
NGVS J12:29:41.39+11:34:19.3	−8.29	0.20	−9.23	0.07	−9.77	0.05	−9.97	0.04	−10.16	0.39	5.9
NGVS J12:29:44.09+12:48:19.6	−7.28	0.01	−8.37	0.03	−8.78	0.01	−8.98	0.01	−9.16	0.07	5.5
NGVS J12:29:53.00+11:57:44.3	−7.98	0.00	−9.09	0.04	−9.64	0.10	−9.87	0.20	−10.06	0.01	5.9
NGVS J12:29:56.34+13:13:12.3	−9.87	0.11	−10.88	0.05	−11.27	0.03	−11.56	0.09	−11.74	0.12	6.6
NGVS J12:29:58.26+13:16:20.8	−7.49	0.75	−8.62	0.05	−9.07	0.17	−9.31	0.69	−9.17	0.00	5.6
NGVS J12:30:01.15+13:07:04.9	−5.81	0.00	−7.01	0.04	−7.24	0.01	−7.84	0.94	−6.71	0.00	5.1
NGVS J12:30:06.21+12:41:18.4	−6.57	0.03	−7.49	0.03	−8.18	0.13	−8.64	0.01	−8.50	0.30	5.4
NGVS J12:30:07.86+12:23:19.9	−6.25	0.05	−7.23	0.01	−7.53	0.08	−7.87	0.01	−7.84	0.06	5.1
NGVS J12:30:10.88+12:11:43.6	−8.66	0.07	−9.67	0.12	−10.18	0.06	−10.39	0.10	−10.54	0.12	6.1
NGVS J12:30:15.99+13:18:27.6	−6.82	0.02	−7.64	0.06	−8.05	0.08	−8.26	0.01	−8.40	0.12	5.2
NGVS J12:30:17.42+12:19:42.8	−12.17	0.02	−15.03	0.03	−14.88	0.01	−15.89	0.01	−15.34	0.03	8.3
NGVS J12:30:32.18+12:51:51.2	−8.20	0.00	−6.30	1.33	−6.74	0.14	−7.23	0.58	−6.34	0.00	4.8
NGVS J12:30:40.41+12:37:17.8	−6.11	0.02	−6.68	0.02	−7.00	0.03	−7.21	0.04	−7.48	0.04	4.8
NGVS J12:30:50.59+12:44:11.7	−8.39	0.03	−9.45	0.09	−9.90	0.11	−10.13	0.14	−10.22	0.04	6.0
NGVS J12:31:10.42+13:05:50.5	−9.06	0.03	−10.13	0.06	−10.63	0.05	−10.82	0.07	−10.94	0.04	6.3
NGVS J12:31:15.73+12:19:54.4	−11.21	0.04	−12.52	0.02	−13.06	0.03	−13.37	0.03	−13.54	0.03	7.3
NGVS J12:31:18.87+13:19:54.7	−6.56	0.47	−7.86	0.32	−8.35	0.04	−8.54	0.07	−8.76	0.01	5.3
NGVS J12:31:19.43+12:44:16.9	−9.46	0.00	−10.43	0.01	−10.86	0.05	−11.09	0.01	−11.22	0.00	6.4
NGVS J12:31:31.68+11:36:11.1	−8.71	0.32	−9.69	0.10	−10.29	0.15	−10.49	0.15	−10.66	0.11	6.1
NGVS J12:31:32.54+11:37:29.1	−12.61	0.04	−14.22	0.03	−14.46	0.03	−15.33	0.03	−15.87	0.04	8.1
NGVS J12:31:33.35+12:03:49.7	−8.71	0.00	−9.67	0.04	−10.06	0.01	−10.41	0.18	−10.48	0.00	6.1
NGVS J12:31:33.92+12:04:03.2	−7.23	0.12	−8.20	0.42	−8.67	0.09	−8.91	0.31	−9.09	0.19	5.5
NGVS J12:31:38.75+11:49:44.7	−7.20	0.10	−8.24	0.05	−8.64	0.12	−8.92	0.07	−9.09	0.06	5.5
NGVS J12:31:51.33+12:39:25.2	−9.63	0.03	−10.78	0.07	−11.30	0.08	−11.54	0.09	−11.67	0.03	6.5
NGVS J12:31:52.01+12:28:54.5	−9.58	0.09	−10.76	0.08	−11.27	0.09	−11.49	0.12	−11.60	0.03	6.5
NGVS J12:31:52.90+12:15:59.1	−10.64	0.00	−12.18	0.08	−12.41	0.01	−13.10	0.06	−13.22	0.02	7.2
NGVS J12:31:53.09+13:15:44.1	−7.02	1.20	−7.39	1.01	−7.91	0.85	−8.39	0.96	−8.59	1.19	5.3
NGVS J12:31:55.93+12:10:27.0	−5.60	0.00	−9.29	0.07	−9.71	0.13	−9.98	0.10	−10.10	0.04	5.9
NGVS J12:31:56.40+11:58:21.6	−7.55	0.21	−8.58	0.19	−9.07	0.05	−9.31	0.12	−9.39	0.05	5.7
NGVS J12:32:00.75+12:37:13.2	−7.76	0.00	−8.82	0.01	−9.23	0.01	−9.50	0.01	−9.61	0.00	5.7
NGVS J12:32:02.74+11:53:24.3	−9.72	0.12	−10.77	0.10	−11.16	0.04	−11.59	0.14	−11.78	0.03	6.6
NGVS J12:32:05.63+11:49:03.6	−8.90	0.03	−9.28	0.04	−9.05	0.02	−9.27	0.60	−9.01	0.04	5.6
NGVS J12:32:09.31+12:50:20.2	−8.54	0.00	−9.46	0.01	−9.92	0.01	−10.17	0.01	−10.23	0.00	6.0
NGVS J12:32:10.50+13:25:09.7	−11.81	0.03	−12.69	0.07	−12.81	0.14	−12.98	0.12	−13.10	0.02	7.1
NGVS J12:32:11.36+12:30:24.9	−6.46	0.00	−7.95	0.01	−8.47	0.01	−8.74	0.01	−8.10	1.38	5.4
NGVS J12:32:12.24+12:03:41.5	−8.88	0.00	−10.00	0.01	−10.41	0.01	−10.82	0.01	−10.90	0.00	6.3
NGVS J12:32:39.99+11:53:43.7	−5.87	0.00	−6.58	0.42	−7.14	0.07	−7.22	0.07	−7.17	0.18	4.8
NGVS J12:32:50.56+12:08:20.8	−7.61	0.06	−8.60	0.21	−9.02	0.01	−9.25	0.54	−9.50	0.05	5.6
NGVS J12:33:05.99+11:32:01.3	−5.97	0.05	−7.51	0.07	−7.82	0.15	−8.18	0.09	−8.37	0.05	5.2
NGVS J12:33:06.41+13:18:11.1	−7.57	0.07	−8.80	0.07	−9.23	0.07	−9.48	0.10	−9.54	0.08	5.7
NGVS J12:33:07.52+12:12:13.4	−6.98	0.00	−7.84	0.06	−8.32	0.03	−8.51	0.01	−8.66	0.12	5.3
NGVS J12:33:10.17+12:05:09.9	−8.29	0.05	−9.35	0.16	−9.82	0.03	−10.12	0.14	−10.13	0.07	6.0
NGVS J12:33:14.01+12:51:28.2	−7.88	0.01	−9.03	0.01	−9.56	0.01	−9.86	0.01	−9.96	0.00	5.9
NGVS J12:33:40.31+12:44:13.6	−9.70	0.03	−10.83	0.04	−11.34	0.04	−11.57	0.05	−11.66	0.03	6.6
NGVS J12:33:40.81+12:34:16.4	−8.04	0.20	−8.96	0.09	−9.64	0.01	−10.14	0.08	−9.73	0.00	6.0
NGVS J12:33:44.70+11:40:57.1	−7.48	0.15	−8.78	0.15	−9.36	0.34	−10.23	0.09	−10.36	0.24	6.0
NGVS J12:33:47.06+11:46:53.8	−8.34	0.54	−9.17	0.35	−9.73	0.28	−9.93	0.37	−10.00	0.30	5.9
NGVS J12:33:48.67+12:46:48.1	−9.29	0.03	−10.43	0.06	−10.95	0.05	−11.21	0.08	−11.27	0.03	6.4
NGVS J12:33:49.57+13:02:20.3	−5.72	0.00	−7.02	0.33	−7.54	0.29	−7.75	0.52	−7.69	0.00	5.0
NGVS J12:33:51.12+12:57:30.3	−7.52	0.07	−8.47	0.13	−8.92	0.13	−9.19	0.42	−9.28	0.13	5.6
NGVS J12:34:01.39+12:43:11.2	−6.08	0.10	−7.09	0.01	−7.50	0.01	−7.79	0.02	−7.78	0.06	5.0
NGVS J12:34:06.56+11:50:12.1	−9.02	0.05	−10.17	0.12	−10.67	0.01	−10.98	0.10	−11.05	0.03	6.3
NGVS J12:34:06.74+12:44:29.7	−9.56	0.10	−10.68	0.03	−11.18	0.03	−11.38	0.04	−11.43	0.08	6.5
NGVS J12:34:07.83+11:45:48.1	−7.91	0.00	−8.86	0.01	−9.22	0.01	−9.60	0.01	−9.74	0.00	5.8
NGVS J12:34:08.98+12:44:24.8	−5.70	0.10	−6.77	0.01	−7.04	0.03	−7.30	0.04	−7.27	0.12	4.8

ORCID iDs

Rubén Sánchez-Janssen https://orcid.org/0000-0003-4945-0056
Laura Ferrarese https://orcid.org/0000-0002-8224-1128
Eric W. Peng https://orcid.org/0000-0002-2073-2781
Joel Roediger https://orcid.org/0000-0002-0363-4266
John P. Blakeslee https://orcid.org/0000-0002-5213-3548
Eric Emsellem https://orcid.org/0000-0002-6155-7166
Thomas H. Puzia https://orcid.org/0000-0003-0350-7061
Chelsea Spengler https://orcid.org/0000-0002-1685-4284
James Taylor https://orcid.org/0000-0002-6639-4183
Alessandro Boselli https://orcid.org/0000-0002-9795-6433
Michele Cantiello https://orcid.org/0000-0003-2072-384X
Patrick Durrell https://orcid.org/0000-0001-9427-3373
Sungsoon Lim https://orcid.org/0000-0002-5049-4390
Chengze Liu https://orcid.org/0000-0002-4718-3428
Simona Mei https://orcid.org/0000-0002-2849-559X
J. Christopher Mihos https://orcid.org/0000-0002-7089-8616
Sanjaya Paudel https://orcid.org/0000-0003-2922-6866
Mathieu Powalka https://orcid.org/0000-0002-1218-3276
Elisa Toloba https://orcid.org/0000-0001-6443-5570

References

Agarwal, M., & Milosavljević, M. 2011, ApJ, 729, 35
Ahn, C. P., Seth, A. C., den Brok, M., et al. 2017, ApJ, 839, 72
Antonini, F. 2013, ApJ, 763, 62
Antonini, F., Barausse, E., & Silk, J. 2015, ApJ, 812, 72
Arca-Sedda, M., & Capuzzo-Dolcetta, R. 2014, MNRAS, 444, 3738
Ashman, K. M., & Zepf, S. E. 2001, AJ, 122, 1888
Behroozi, P. S., Wechsler, R. H., Lu, Y., et al. 2013, ApJ, 787, 156
Bekki, K. 2007, PASA, 24, 77
Bekki, K., & Chiba, M. 2004, A&A, 417, 437
Bekki, K., Couch, W. J., & Shioya, Y. 2006, ApJL, 642, L133
Bekki, K., Forbes, D., Beasley, M., & Couch, W. 2003, MNRAS, 344, 1334
Bekki, K., & Freeman, K. C. 2003, MNRAS, 346, 11
Bellazzini, M., Ibata, R. A., Chapman, S. C., et al. 2008, AJ, 136, 1147
Binggeli, B., & Cameron, L. 1991, A&A, 252, 27
Binggeli, B., Tammann, G., & Sandage, A. 1987, AJ, 94, 251
Blakeslee, J., Jordán, A., Mei, S., et al. 2009, ApJ, 694, 556
Böker, T., Laine, S., van der Marel, R. P., et al. 2002, AJ, 123, 1389
Brook, C. B., Cintio, A. D., Knebe, A., et al. 2014, ApJL, 784, L14
Bullock, J. S., & Johnston, K. V. 2005, ApJ, 635, 931
Capuzzo-Dolcetta, R. 1993, ApJ, 415, 616
Capuzzo-Dolcetta, R., & Miocchi, P. 2008a, ApJ, 681, 1136
Capuzzo-Dolcetta, R., & Miocchi, P. 2008b, MNRAS, 388, L69
Carollo, C. M., Stiavelli, M., & Mack, J. 1998, AJ, 116, 68
Carollo, D., Beers, T. C., Chiba, M., et al. 2010, ApJ, 712, 692
Carson, D. J., Barth, A. J., Seth, A. C., et al. 2015, AJ, 149, 170
Cen, R. 2001, ApJL, 549, L195
Chiboucas, K., Jacobs, B. a., Tully, R. B., & Karachentsev, I. D. 2013, AJ, 146, 126
Chilingarian, I. V., Cayatte, V., & Bergond, G. 2008, MNRAS, 390, 906
Chilingarian, I. V., & Mamon, G. A. 2008, MNRAS, 385, 83
Conroy, C., Gunn, J. E., & White, M. 2009, ApJ, 699, 486
Cooper, A. P., Cole, S., Frenk, C. S., et al. 2010, MNRAS, 406, 744
Cote, P., Blakeslee, J. P., Ferrarese, L., et al. 2004, ApJS, 153, 223
Cote, P., Ferrarese, L., Jordan, A., et al. 2007, ApJ, 671, 1456
Cote, P., Piatek, S., Ferrarese, L., et al. 2006, ApJS, 165, 57
Courteau, S., Widrow, L. M., McDonald, M., et al. 2011, ApJ, 739, 20
Dalal, N., White, M., Bond, J. R., & Shirokov, A. 2008, ApJ, 687, 12
Deason, A. J., Belokurov, V., & Weisz, D. R. 2015, MNRAS, 448, L77
Deason, A. J., Mao, Y.-Y., & Wechsler, R. H. 2016, ApJ, 821, 5
De Propris, R., Phillipps, S., Drinkwater, M., et al. 2005, ApJL, 623, L105
den Brok, M., Peletier, R. F., Seth, A., et al. 2014, MNRAS, 445, 2385
Diemand, J., Madau, P., & Moore, B. 2005, MNRAS, 364, 367
Drinkwater, M., Jones, J., Gregg, M., & Phillipps, S. 2000, PASA, 17, 227
Drinkwater, M. J., Gregg, M. D., Hilker, M., et al. 2003, Natur, 423, 519
El-Badry, K., Wetzel, A., Geha, M., et al. 2016, ApJ, 820, 131
Elmegreen, B. G., & Efremov, Y. N. 1997, ApJ, 480, 235
Emsellem, E., & van de Ven, G. 2008, ApJ, 674, 653
Evstigneeva, E. A., Gregg, M. D., Drinkwater, M. J., & Hilker, M. 2007, AJ, 133, 1722
Fattahi, A., Navarro, J. F., Sawala, T., et al. 2016, MNRAS, 457, 844
Ferrarese, L., Côté, P., Cuillandre, J.-C., et al. 2012, ApJS, 200, 4
Ferrarese, L., Côté, P., Dalla Bontà, E., et al. 2006a, ApJL, 644, L21
Ferrarese, L., Côté, P., Jordán, A., et al. 2006b, ApJS, 164, 334
Ferrarese, L., Côté, P., Sánchez-Janssen, R., et al. 2016, ApJ, 824, 10
Fiorentino, G., Bono, G., Monelli, M., et al. 2014, ApJL, 798, L12
Fuentes-Carrera, I., Jablonka, P., Sarajedini, A., et al. 2008, A&A, 483, 769
Gao, L., Springel, V., & White, S. D. M. 2005, MNRAS, 363, L66
Georgiev, I., Böker, T., Leigh, N., Lützgendorf, N., & Neumayer, N. 2016, MNRAS, 457, 2122
Georgiev, I., Puzia, T., Goudfrooij, P., & Hilker, M. 2010, MNRAS, 406, 1967
Georgiev, I. Y., & Böker, T. 2014, MNRAS, 441, 3570
Georgiev, I. Y., Hilker, M., Puzia, T. H., Goudfrooij, P., & Baumgardt, H. 2009, MNRAS, 396, 1075
Glass, L., Ferrarese, L., Côté, P., et al. 2011, ApJ, 726, 31
Gnedin, O. Y., Ostriker, J. P., & Tremaine, S. 2014, ApJ, 785, 71
Goerdt, T., Moore, B., Kazantzidis, S., et al. 2008, MNRAS, 385, 2136
Graham, A. W., & Spitler, L. R. 2009, MNRAS, 397, 2148
Grossauer, J., Taylor, J. E., Ferrarese, L., et al. 2015, ApJ, 807, 88
Guillard, N., Emsellem, E., & Renaud, F. 2016, MNRAS, 461, 3620
Haçegan, M., Jordán, A., Côté, P., et al. 2005, ApJ, 627, 203
Harris, W. E., & Pudritz, R. E. 1994, ApJ, 429, 177
Hartmann, M., Debattista, V. P., Seth, A., Cappellari, M., & Quinn, T. R. 2011, MNRAS, 418, 2697
Hau, G. K. T., Spitler, L. R., Forbes, D. A., et al. 2009, MNRAS, 394, 97
Hilker, M., Infante, L., Vieira, G., Kissler-Patig, M., & Richtler, T. 1999, A&AS, 134, 75
Hilker, M., & Richtler, T. 2000, A&A, 362, 895
Hopkins, P. F., Murray, N., Quataert, E., & Thompson, T. A. 2009, MNRAS, 401, L19
Hudson, M. J., Harris, G. L., & Harris, W. E. 2014, ApJL, 787, L5
Ibata, R. A., Gilmore, G., & Irwin, M. J. 1994, Natur, 370, 194
Ibata, R. A., Gilmore, G., & Irwin, M. J. 1995, MNRAS, 277, 781
Jordan, A., McLaughlin, D. E., Cote, P., et al. 2007, ApJS, 171, 101
Karachentsev, I. D., Makarov, D. I., & Kaisina, E. I. 2013, AJ, 145, 101
Kruijssen, J. M. D. 2015, MNRAS, 454, 1658
Kruijssen, J. M. D., Pelupessy, F. I., Lamers, H. J. G. L. M., Portegies Zwart, S. F., & Icke, V. 2011, MNRAS, 414, 1339
Lacerna, I., & Padilla, N. 2011, MNRAS, 412, 1283
Lauer, T. R., Faber, S. M., Ajhar, E. A., Grillmair, C. J., & Scowen, P. A. 1998, AJ, 116, 2263
Lee, Y.-W., Joo, J.-M., Sohn, Y.-J., et al. 1999, Natur, 399, A7
Licquia, T. C., & Newman, J. A. 2015, ApJ, 806, 96
Lisker, T., Grebel, E. K., Binggeli, B., & Glatt, K. 2007, ApJ, 660, 1186
Lisker, T., Janz, J., Hensler, G., et al. 2009, ApJL, 706, L124
Liu, C., Peng, E. W., Côté, P., et al. 2015a, ApJ, 812, 34
Liu, C., Peng, E. W., Toloba, E., et al. 2015b, ApJL, 812, L2
Liu, Y., Peng, E. W., Blakeslee, J., et al. 2016, ApJ, 818, 179
Lotz, J., Miller, B., & Ferguson, H. 2004, ApJ, 613, 262
Lotz, J. M., Telford, R., Ferguson, H. C., et al. 2001, ApJ, 552, 572
Ma, J., De Grijs, R., Chen, D., et al. 2007, MNRAS, 376, 1621
Mackey, A. D., & van den Bergh, S. 2005, MNRAS, 360, 631
Mateo, M. 1998, ARA&A, 36, 435
McConnell, N. J., & Ma, C.-P. 2013, ApJ, 764, 184
McLaughlin, D. E. 1999, AJ, 117, 2398
Mclaughlin, D. E., King, A. R., & Nayakshin, S. 2006, ApJ, 650, 37
Mei, S., Blakeslee, J., Côté, P., et al. 2007, ApJ, 655, 144
Meylan, G., Sarajedini, A., Jablonka, P., et al. 2001, AJ, 122, 830
Mieske, S., Hilker, M., Jordán, A., et al. 2008, A&A, 487, 921
Mieske, S., Hilker, M., & Misgeld, I. 2012, A&A, 537, A3
Mieske, S., Jordán, A., Côté, P., et al. 2006, ApJ, 653, 193
Mihos, J. C., & Hernquist, L. 1994, ApJL, 437, L47
Miller, B. P., Gallo, E., Greene, J. E., et al. 2015, ApJ, 799, 98
Miller, B. W., Lotz, J. M., Ferguson, H. C., Stiavelli, M., & Whitmore, B. C. 1998, ApJL, 508, L133
Milosavljevič, M., & Bromm, V. 2014, MNRAS, 440, 50
Mistani, P. A., Sales, L. V., Pillepich, A., et al. 2015, MNRAS, 455, 2323
Monaco, L., Bellazzini, M., Ferraro, F. R., & Pancino, E. 2005, MNRAS, 356, 1396
Monaco, L., Saviane, I., Perina, S., et al. 2009, A&A, 502, L9
Moster, B. P., Naab, T., & White, S. D. M. 2013, MNRAS, 428, 3121
Muñoz, R. R. P., Eigenthaler, P., Puzia, T. H. T., et al. 2015, ApJL, 813, L15
Nguyen, D. D., Seth, A. C., Neumayer, N., et al. 2018, ApJ, 858, 118N

Norris, J., & Da Costa, G. 1995, ApJ, 447, 680
Norris, J. E., Freeman, K. C., Mayor, M., & Seitzer, P. 1997, ApJL, 487, L187
Norris, M., Kannappan, S., Forbes, D., et al. 2014, MNRAS, 443, 1151
Noyola, E., Gebhardt, K., Kissler-Patig, M., et al. 2010, ApJL, 719, L60
Oman, K. A., Hudson, M. J., & Behroozi, P. S. 2013, MNRAS, 431, 2307
Ordenes-Briceño, Y., Puzia, T. H., Eigenthaler, P., et al. 2018, ApJ, 860, 4
Pancino, E., Ferraro, F. R., Bellazzini, M., Piotto, G., & Zoccali, M. 2000, ApJL, 534, L83
Paudel, S., Lisker, T., & Kuntschner, H. 2011, MNRAS, 413, 1764
Peng, E. W., Jordan, A., Cote, P., et al. 2008, ApJ, 681, 197
Pfeffer, J., & Baumgardt, H. 2013, MNRAS, 433, 1997
Pfeffer, J., Hilker, M., Baumgardt, H., & Griffen, B. F. 2016, MNRAS, 458, 2492
Pfeffer, J., Kruijssen, J. M. D., Crain, R. A., & Bastian, N. 2018, MNRAS, 475, 4309
Puzia, T. H., & Sharina, M. E. 2008, ApJ, 674, 909
Ricotti, M., Parry, O. H., & Gnedin, N. Y. 2016, ApJ, 831, 204
Rodriguez-Gomez, V., Pillepich, A., Sales, L. V., et al. 2016, MNRAS, 458, 2371
Roediger, J. C., Ferrarese, L., Côté, P., et al. 2017, ApJ, 836, 120
Rossa, J., van der Marel, R. P., Böker, T., et al. 2006, AJ, 132, 1074
Sánchez-Janssen, R., & Aguerri, J. A. L. 2012, MNRAS, 424, 2614
Sánchez-Janssen, R., Ferrarese, L., MacArthur, L. A., et al. 2016, ApJ, 820, 69
Sandoval, M. A., Vo, R. P., Romanowsky, A. J., et al. 2015, ApJL, 808, L32
Sarajedini, A., & Layden, A. C. 1995, AJ, 109, 1086
Sawala, T., Frenk, C. S., Fattahi, A., et al. 2015, MNRAS, 448, 2941
Scott, N., & Graham, A. W. 2013, ApJ, 763, 76
Sérsic, J. 1968, Atlas de Galaxias Australes (Cordoba: Observatorio Astronomico)
Seth, A. C., Cappellari, M., Neumayer, N., et al. 2010, ApJ, 714, 713
Seth, A. C., Dalcanton, J. J., Hodge, P. W., & Debattista, V. P. 2006, AJ, 132, 2539
Seth, A. C., van den Bosch, R., Mieske, S., et al. 2014, Natur, 513, 398
Sick, J., Courteau, S., Cuillandre, J.-C., et al. 2014, in IAU Symp. 311, Galaxy Masses as Contraints of Formation Models (Cambridge: Cambridge Univ. Press), 82
Smith, R., Sánchez-Janssen, R., Beasley, M., et al. 2015, MNRAS, 454, 2502
Smith, R., Sanchez-Janssen, R., Fellhauer, M., et al. 2013, MNRAS, 429, 1066
Spengler, C., Côté, P., Roediger, J., et al. 2017, ApJ, 849, 55
Spitler, L., & Forbes, D. 2009, MNRAS, 392, L1
Tremaine, S. D., Ostriker, J. P., & Spitzer, L., Jr. 1975, ApJ, 196, 407
Turner, M. L., Côté, P., Ferrarese, L., et al. 2012, ApJS, 203, 5
van de Ven, G., van den Bosch, R. C. E., Verolme, E. K., & de Zeeuw, P. T. 2006, A&A, 445, 513
van den Bergh, S., & Mackey, A. D. 2004, MNRAS, 354, 713
van den Bosch, F. C., Jiang, F., Hearin, A., et al. 2014, MNRAS, 445, 1713
van Oirschot, P., Starkenburg, E., Helmi, A., & Nelemans, G. 2017, MNRAS, 464, 863
Volonteri, M. 2010, A&ARv, 18, 279
Walcher, C.-J., Boeker, T., Charlot, S., et al. 2006, ApJ, 649, 692
Walcher, C. J., van der Marel, R. P., McLaughlin, D., et al. 2005, ApJ, 618, 237
Watson, D. F., & Conroy, C. 2013, ApJ, 772, 139
Wechsler, R. H., Bullock, J. S., Primack, J. R., Kravtsov, A. V., & Dekel, A. 2002, ApJ, 568, 52
Wechsler, R. H., Zentner, A. R., Bullock, J. S., Kravtsov, A. V., & Allgood, B. 2006, ApJ, 652, 71
Wehner, E. H., & Harris, W. E. 2006, ApJL, 644, L17
Woo, J., Courteau, S., & Dekel, A. 2008, MNRAS, 390, 1453
Yong, D., Da Costa, G. S., & Norris, J. E. 2016, MNRAS, 460, 1846
Zhang, H.-X., Peng, E. W., Cote, P., et al. 2015, ApJ, 802, 30
Zhang, H.-X., Puzia, T. H., & Weisz, D. R. 2017, ApJS, 233, 13
Zolotov, A., Willman, B., Brooks, A. M., et al. 2009, ApJ, 702, 1058